

ANALYTICAL AND EXPERIMENTAL STUDIES OF
SOUND PRESSURES ON DUCTED
PROPELLERS

REPORT NO. 9500-950001

DECEMBER 1966

by

W. Fricke, J.R. Bissell, W.T. Bamberg, C.K. Martina

Final Report

NASA Contract NASW-1217

Prepared for

The National Aeronautics and Space Administration
Washington, D.C.

FOREWORD

This report has been prepared by the Bell Aerosystems Company under NASA Contract No. NASw-1217, entitled: Analytical and Experimental Studies of Sound Pressures on Ducted Propellers. Dr. Werner Fricke, Structural Systems Department, was the technical director, supported by Messrs. W. J. Bamberg and J. R. Bissell, Integrated Systems Department, and by Mr. C. K. Martina, Engineering Laboratory. The contract was monitored by Mr. C. E. Watkins, NASA-Langley, who made many constructive comments and suggestions, in particular during the analytical phase of the study. The wind tunnel experiments were conducted in the large scale wind tunnel of the NASA-Ames Research Center with Mr. Kenneth W. Mort assigned to the propulsion tests. The support given by Messrs. C. E. Watkins and Kenneth W. Mort during the course of the study is gratefully acknowledged.

CONTENTS

Section		Page
	SUMMARY	1
I	INTRODUCTION	2
II	ANALYSIS	4
	A. Introduction	4
	B. Description	4
III	EXPERIMENTS	6
	A. Design of Full-Scale Model	6
	B. Acoustic Instrumentation	9
	1. Introduction	9
	2. Microphone Selection	10
	3. Associated Instrumentation for Recording and Monitoring	10
	4. Calibration	11
	C. Propulsion Instrumentation	11
	D. Test Program	18
IV	RESULTS OF EXPERIMENTS	20
	A. Introduction	20
	B. Recorded Sound-Pressure Time Functions	20
	C. Harmonic Analysis	28
	D. Effect of Tip Clearance on Sound Pressure	33
	E. Radial Sound Pressure Field, Test Results	38
V	COMPARISON OF TEST RESULTS WITH THE CALCULATED VALUES	44
VI	CONCLUSIONS	52
VII	RECOMMENDATIONS	53
VIII	REFERENCES	54
IX	APPENDIX	55
	A. Introduction	55
	B. Model	55
	C. Solution	56
	D. Some Aids to Evaluation	64

ILLUSTRATIONS

Figure		Page
1	Cross Section of Fiberglass Duct with Mounted Test Rig	7
2	Ducted Propeller and Test Rig	8
3	Block Diagram of Acoustic Instrumentation	12
4	Instrumentation Setup	13
5	Scale Model on Tunnel Floor	15
6	Schematic of Motor Suspension for Measuring Propeller Thrust and Torque	16
7	Sound Pressure-Time Function (Run No. 8, N = 1000 rpm, $\beta = 17^\circ$),	21
8	Sound Pressure-Time Function (Run No. 8, N = 2000 rpm, $\beta = 17^\circ$),	22
9	Sound Pressure-Time Function (Run No. 8, N = 1000 rpm, $\beta = 17^\circ$),	24
10	Sound Pressure-Time Function (Run No. 8, N = 2000 rpm, $\beta = 17^\circ$),	25
11	Acceleration Spectrum (Run No. 4, N = 1500 rpm, $\beta = 41^\circ$),	26
12	Acceleration Spectrum (Run No. 8, N = 2400 rpm, $\beta = 17^\circ$),	27
13	Recorded and Normalized Sound Pressure-Time Functions at Six Microphone Positions (Run No. 8, N = 2400 rpm)	29
14	Sound Pressure Spectrum (Run No. 8, N = 1000, 2400 rpm, - $\beta = 17^\circ$, Mic. 2)	30
15	Sound Pressure Spectrum (Run No. 8, N = 1000, 2400 rpm, $\beta = 17^\circ$, Mic. 3)	31
16	Sound Pressure Spectrum (Run No. 8, N = 2400 rpm, $\beta = 17^\circ$, Mic. 5)	32
17	Effect of Tip Clearance on Overall Sound Pressure (Data from Runs 6, 11, and 12)	34
18	Sound Pressure-Time Function (Run No. 12, $\Delta R = 3/8$ in., N = 1500 rpm, $\beta = 23^\circ$)	35
19	Sound Pressure-Time Function (Run No. 11, $\Delta R = 1.5$ in., N = 1500 rpm, $\beta = 23^\circ$)	36
20	Effect of Tip Clearance on Peak to Peak Sound Pressure (Data from Runs 6, 11, and 12)	37
21	Sound Pressure-Radial Distance Function(Run No. 15, N = 1500 rpm, $\beta = 17^\circ$, Mic. 5)	39
22	Sound Pressure-Radial Distance Function(Run No. 15, N = 2000 rpm, $\beta = 17^\circ$, Mic. 5)	40
23	Sound Pressure Spectrum(Run No. 15, N = 2000 rpm, $\beta = 17^\circ$ Mic. 5, at Duct Wall).	41

ILLUSTRATIONS (CONT)

Figure		Page
24	Sound Pressure Spectrum(Run No. 15, N = 2000 rpm, $\beta = 17^\circ$ Mic. 5 Extended 9 in.)	42
25	Sound Pressure Spectrum(Run No. 15, N = 2000 rpm, $\beta = 17^\circ$ Mic 5 Extended 30 in.)	43
26	Sound Pressure Level Distribution Along the Duct Inner Surface (Run No. 6, $\beta = 23^\circ$)	45
27	Sound Pressure Level Distribution Along the Duct Inner Surface (Run No. 8, $\beta = 17^\circ$)	46
28	Sound Pressure Level Distribution Along the Duct Inner Surface (Run No. 10, $\beta = 29^\circ$)	47
29	Radial Variation of Sound Pressure Level (Run No. 15, $\beta = 17^\circ$, Mic. 5)	49
30	Harmonic Content(Run No. 8, $\beta = 17^\circ$, Mic. 2)	50
31	Harmonic Content(Run No. 8, $\beta = 29^\circ$, Mic. 2)	51
32	Propeller Disk and Coordinate System	57

TABLES

Number		Page
I	Characteristic Numbers and Coefficients for Bessel Functions . .	65
II	Fourier-Bessel Coefficients	66

LIST OF SYMBOLS OF THE APPENDIX

a	-	arbitrary constant
$\bar{a}_{m\mu}$	-	amplitude coefficient
A_B	-	propeller blade planform area
A'_{mk}	-	arbitrary constant
b	-	arbitrary constant
\bar{b}	-	propeller blade mean chord
$\bar{b}_{m\mu}$	-	amplitude coefficient
B	-	number of propeller blades
B'_{mk}	-	arbitrary constant
c	-	speed of sound
E_m	-	modified Bessel function, $J_m + Q_{mk} Y_m$
Q_{mk}	-	B'_{mk}/A'_{mk}
J_m	-	Bessel function of the first kind, order m
k	-	characteristic number in argument of Bessel function
m	-	nB , order of Bessel function
n	-	angular harmonic
P	-	sound pressure
P_o	-	pressure over propeller blades
q	-	nondimensional separation constant
r	-	radial ordinate
\bar{r}	-	radial ordinate of the center of pressure
R	-	characteristic function
R_H	-	hub radius
R_S	-	duct inner surface radius
t	-	time
T_P	-	propeller thrust
X	-	characteristic x function
Y_m	-	Bessel function of the second kind order m

LIST OF SYMBOLS (CONT)

x	-	axial ordinate
β_e	-	effective or equivalent blade angle
γ	-	included angle of propeller blade sector
θ	-	angular ordinate
μ	-	rank of the root k
ϕ	-	phase angle
ω	-	propeller angular velocity

SUMMARY

An analytical approach for the prediction of rotational sound due to blade loadings in the duct of ducted propellers has been developed, based on definable propulsion quantities. Tests were conducted on a full-scale model of a 3-blade, ducted propeller. A comparison of the experimental data with those analytically predicted showed the following results:

The calculated and measured overall sound pressure levels at the propeller plane and along the inner wall of the duct are in good agreement, with some deviations not exceeding 2db. Therefore, the analytical approach is a satisfactory tool for predicting the overall sound pressure distribution along the duct wall.

A comparison of the calculated and measured sound pressures of the higher harmonics show different decays. This may be attributed to the rectangular blade pressure distribution, radial and chordwise, assumed in the analysis.

The radial decay of the measured and calculated sound pressure behind the propeller plane is similar in the region near the duct wall, but differs when approaching the hub surface. This effect may be explained by a turbulent wake found to exist in this region by a flow velocity survey.

An additional experimental study was conducted on the effect of increased tip clearance on sound pressure.

I. INTRODUCTION

Various types of VTOL-aircraft and air cushion vehicles being developed or tested utilize ducted propellers or fans. The application of a duct results in an increase of the propulsion performance at low speed and also in a reduction of the propeller diameter. Furthermore, VTOL-aircraft will benefit from the fact that the asymmetrical blade loadings during the transition from take-off to cruise flight will be reduced by a ducted propeller. Consequently, the interest of designers in the application of ducts increased appreciably within the last few years.

A propeller or fan operating inside a duct produces a pressure pattern rotating with the blades. The resulting periodic pressure fluctuations is the origin of the rotational noise. Two sources contribute to the rotational noise: noise due to thickness of the blades, and noise due to blade loading. For propellers operating at subsonic speed and under normal blade loadings, the blade loading noise is the most pronounced noise source. Under those conditions, thickness noise may be neglected in computing the rotational noise.

The present state-of-the-art allows a reasonably accurate calculation of the lift noise associated with a freely radiating propeller. A bibliography of representative studies conducted on freely radiating propellers is given in References 1, 2, and 3. All these analytical approaches are based on an assumed aerodynamic pressure distribution around the blades. Calculated and measured near field sound pressures are in good agreement. Only limited information exists on sound pressure fields inside ducts. One worth-while study is reported by Tyler and Sofrin (Reference 4). They investigated the behavior of the rotating pressure pattern propagating in a cylindrical compressor duct and describe this in functional forms. The result of that study, however, does not allow an explicit determination of the sound pressures for a given propeller geometry and operating condition.

Another work reported in Reference 5 indicates that free radiating propeller theory (eg. Reference 3) using the "in duct" thrust and torque of the propeller may be used to obtain the sound pressure distribution in the duct. Comparisons between test and theory using calculated blade loadings are in very good agreement for the sound pressure distribution

close to the propeller or compressor plane. Results obtained using measured thrusts and torque are lacking and such results would be of interest since limiting the effects of the duct and centerbody to the blade loadings is somewhat questionable.

Preliminary studies on the sound field inside propeller ducts were also conducted by Bell Aerosystems Company during the development of the SKMR-1 Hydroskimmer and the X-22A aircraft. A semi-empirical method was used to calculate the sound pressures along the inner duct surface, based on the analytical approach applied to a freely radiating propeller as presented by Hubbard and Regier (Reference 3.). The results were corrected for total reflection of the sound waves at the wall surface, assuming a flat surface (Reference 6). Subsequent experiments performed during ground tests of both vehicles showed a fair agreement between calculated and measured data along the leading edge of the duct, but a deviation of the order of 15 db at the trailing edge. No measurements were possible at that time at the propeller plane.

A knowledge of the sound field inside the duct of ducted propellers is required for three reasons:

- (1) To develop design criteria for light weight duct structures of sufficient acoustic fatigue life, in particular for those located in the critical region near the propeller plane.
- (2) To predict the near sound field around the airplane. This is required for estimating the amount of sound proofing of the cockpit and cabin necessary for crew and passenger comfort.
- (3) To predict the far sound field for assessing the community response.

The principal objective of this work was the development of an analytical approach for calculating the sound pressure distribution inside the duct along the inner duct wall and along the radius, using definable propulsion quantities. The validity of this approach had to be confirmed by exploring the sound field in a full-scale model duct under measured operating conditions.

A second objective of this program was the experimental determination of the relation between tip clearance and sound pressure.

II. ANALYSIS

A. INTRODUCTION

In this section, the analytical approach used for calculating sound pressures in a propeller duct unit is described in general terms. The detailed development of the equations is given in the Appendix to this report.

B. DESCRIPTION

The sound pressure field in the plane of the propeller is assumed to be equal to the rotating net blade pressure distribution acting normal to the propeller plane. At any fixed point located in the propeller plane, the fluctuating pressure may be expanded in a Fourier series and expressed:

$$P(r, \theta, t) = \sum_{n=1}^{\infty} P_n(r) \cos [n B (\theta - \omega t) + \phi_{nB}] \quad (1)$$

where

B is the number of blades

n is the harmonic

$P_n(r)$, ϕ_n are the pressure amplitude and phase parameters required to synthesize the particular pressure distribution associated with a given propeller thrust and torque. The only physical restriction to $P_n(r)$ is that its radial gradient $\frac{\partial P_n(r)}{\partial r}$ must be zero at the bounding walls, i.e., there is no flow through the duct walls.

A stationary type solution of the wave equation reveals that for a region bounded by concentric cylindrical walls, the functions required to define $P_n(r)$ and satisfy the conditions of no flow through the duct are combinations of Bessel functions of the first and second kind. A more detailed account is given in the Appendix, but for the present let it be sufficient to state that $P_n(r)$ may be expressed as:

$$P_n(r) = \sum_{\mu=0}^{\infty} a_{nB\mu} E_{nB}(k_{nB\mu} r) \quad (2)$$

where

$E_{nB}(K_{n\mu}, \mu, r)$ is the Bessel function combination and $a_{n\mu}$ are weighting coefficients through which the required distribution is obtained. The symbol μ defines the radial mode.

The solution of the wave equation also shows the axial or x-variation of the sound pressure field to be:

$$e^{-|x|\sqrt{k_{m\mu}^2 - \left(\frac{m\omega}{c}\right)^2}}, \quad m = nB$$

ω is the forcing frequency and $k_{m\mu}$ is proportional to the frequency which would be generated by a wave travelling in free space in a radial direction and with the speed of sound c . $k_{m\mu}$ is considered in greater detail in the Appendix. When the above parameter is real, the pressure field decays exponentially with increasing distance from the propeller plane. If $\frac{m\omega}{c} > k_{m\mu}$, the pressure fluctuations propagate in the duct as a wave of undiminished intensity.

The complete analytical expression for the instantaneous sound pressure is:

$$P = \sum_{m=B}^{\infty} \sum_{\mu=0}^{\infty} a_{m\mu} E_m(k_{m\mu}, r) \cos [m(\theta - \omega t) + \phi_m] e^{-|x|\sqrt{k_{m\mu}^2 - \left(\frac{m\omega}{c}\right)^2}} \quad (3)$$

The propeller blade pressure distribution assumed for the calculated pressures of this report is constant both chordwise and radially, and the propeller blade planform is assumed to be a sector of a circle with an included angle γ . However, the form of the blade pressure distribution and planform is arbitrary, affecting the evaluation of the coefficients $a_{m\mu}$ and the phase angle, ϕ_m .

The evaluation of $a_{m\mu}$ and ϕ_m and the relationship between the blade pressure distribution and the thrust and torque is described in detail in the Appendix.

III. EXPERIMENTS

A. DESIGN OF FULL-SCALE MODEL

The main objective of the study, the development of equations relating the sound pressure along the duct wall with the propulsion quantities, required measuring the sound pressure field at different points of the inner duct wall. It was also desirable to explore during the experimental phase, the radial sound field between duct and centerbody. All these measurements had to be conducted on a model equipped with a duct of a cylindrical inner surface and a cylindrical centerbody so as to be comparable with the mathematical model as described in the analysis. Economic considerations dictated the selection of a full-scale powered model of the X-22A ducted propeller as a basic building frame allowing utilization of existing hardware to a great extent. The model underwent modifications to provide:

- (1) A cylindrical inner duct surface extending from the propeller plane to the trailing edge, with provisions for three flush mounted microphones.
- (2) A cylindrical centerbody fairing.
- (3) A microphone rack attached to the duct for installation of three microphones capable of traversing the sound field radially.

The inner duct liner and centerbody fairing were fabricated of glass cloth and epoxy resin lay-up of three-sixteenth inches thickness, bonded to a wooden framework (Figures 1 and 2). The liner was installed in three interlocking sections and bolted to the original duct for easy removal. The centerbody consisted of two halves to be bolted to the gearbox face flanges. A large cutout in the outer skin of the original duct on the top centerline provided access for mounting the microphone rack to the main beam, the installation of three flush mounted microphones, and the mounting of the microphone terminal board.

In order to install the three fixed microphones, the fiberglass skin was threaded and the microphones were screwed into the skin. A jam nut prevented these microphones from loosening due to structural vibrations. The three movable microphones were

MIC. NO.	STATION
1	2.0
2	6.9
3	11.3
4	20.0
5	41.8
6	50.0

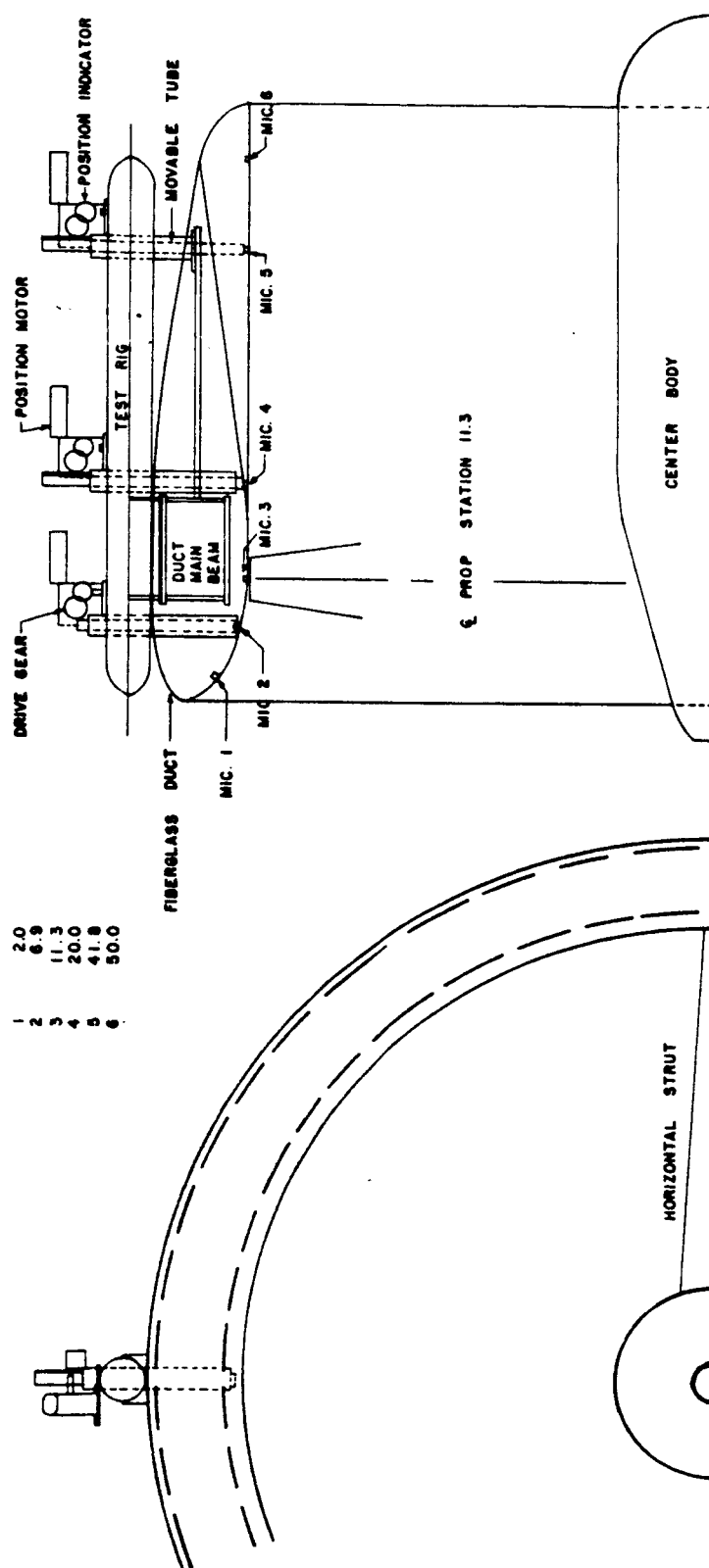


Figure 1. Cross-section of Fiberglass Duct with Mounted Test Rig

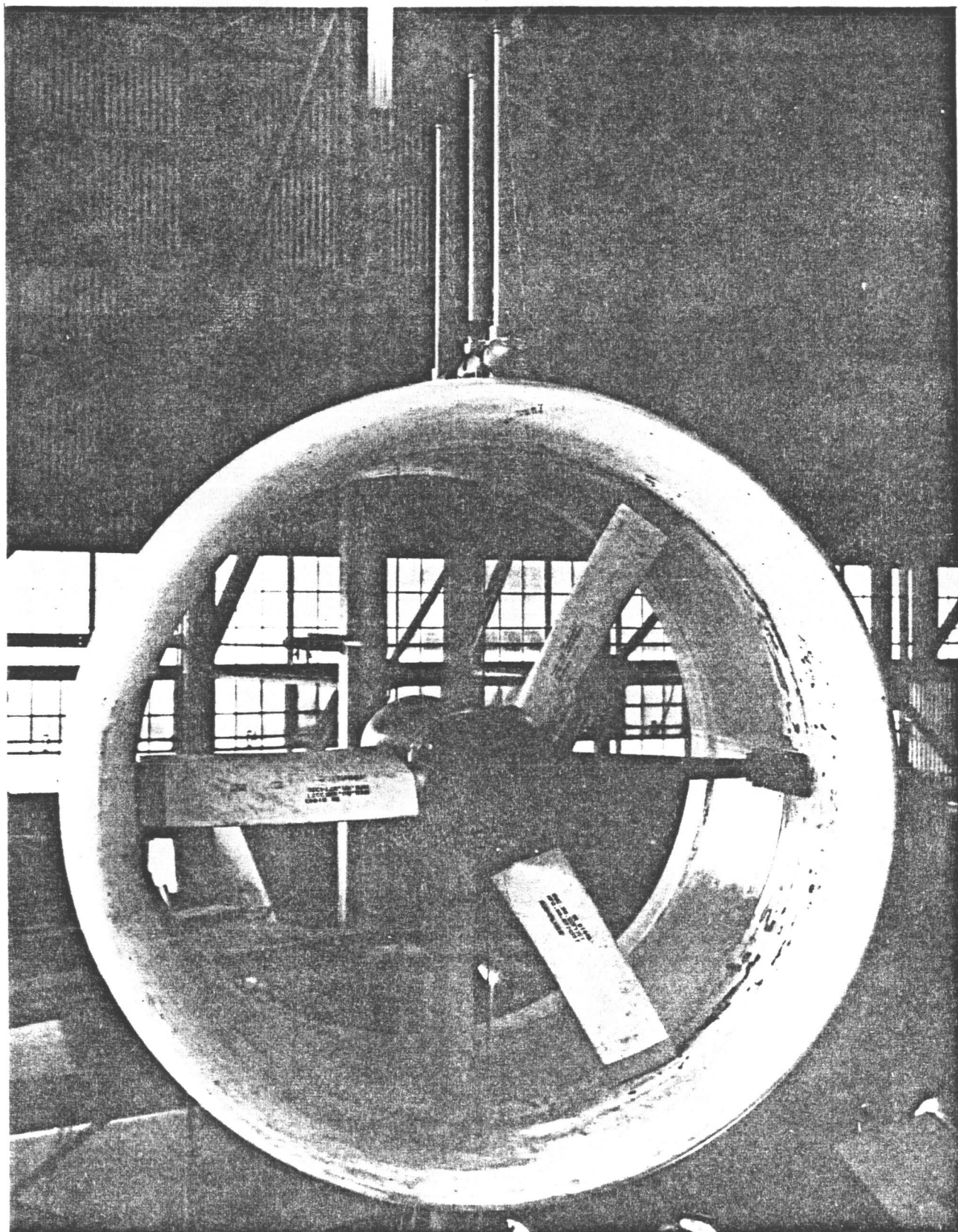


Figure 2. Ducted Propeller and Test Rig

mounted in the ends of steel tubes installed in the microphone rack. Gear racks were attached to the tubes which were driven by 1/15 hp reversible AC-DC-motors with a 745:1 speed ratio that provided the desired speed reduction for remote positioning over a range of approximately 30 inches. Position was indicated by rotary-type potentiometers. Linear ball bearings installed in the tube support mount provided a chatter-free movement of the tubes.

The table below shows the stations of all six microphones, their distance in inches from the propeller plane and also the dimensionless distance $\frac{X}{R_S}$, where $R_S = 42.4$ inches.

Microphone	Station	X [inches]	$\frac{X}{R_S}$
1	2.0	-9.3	-0.219
2	6.9	-4.4	-0.104
3	11.3	0	0
4	20.0	+8.7	+0.205
5	41.8	+30.5	+0.719
6	50.0	+38.7	+0.913

B. ACOUSTIC INSTRUMENTATION

1. Introduction

Special requirements had to be met by the microphone system. The dynamic range of sound pressure levels expected was from 130 to 170 db, depending on operational conditions and on the microphone location. The sensor had to be small in size and of a low impedance output because of the long distance between wind tunnel floor and data recording room.

Previous experience gained by Bell Aerosystems Company during sound pressure measurements on ducted propellers had demonstrated the importance of eliminating spurious signals due to mechanical vibration. Duct vibration can reach values in the order of ± 50 g. Without vibration mounting or vibration compensation by electronic methods, the response of the microphone to mechanical vibration might be of the same order of magnitude as that produced by the sound field.

2. Microphone Selection

After a survey of the performance data of the different microphone types, a microphone built by Kistler Instrument Corporation, Model 717L, was selected. This device combines a quartz-type microphone integrated with a solid-state charge amplifier in one unit. The charge amplifier provides the desired low output impedance (less than 100 ohm). The sensor output can be connected directly to a microphone amplifier, the output of which may then be fed to an AC-voltmeter, sound level meter, analyzer or tape recorder.

Vibration compensation is achieved by mounting, in one unit, a quartz accelerometer in series with the sound pressure sensing element. Both systems generate equal, but opposite signals in response to mechanical vibrations. If crystals with opposite polarities are used and their electrodes connected in parallel, vibration signals can be compensated and a net-sound pressure sensitivity results.

Of course, the vibration compensation is limited due to fabrication tolerances and residual misalignments of the quartz axes. A reduction of the vibration sensitivity at a ratio 100:1 may be obtained with compensated microphones, if compared with an uncompensated microphone of the same pressure sensitivity.

Prior to installation and after completion of the tests, all microphones were subjected to a sinusoidal mechanical vibration up to ± 30 g peak acceleration at 200 cps. The residual vibration sensitivities obtained were then used for a calculation of the errors due to duct vibration recorded during the wind-tunnel test phase (see Section IV).

3. Associated Instrumentation for Recording and Monitoring

To obtain the pressure-time function of each of the microphone outputs and time correlation between each of the six microphones, all output signals were tape recorded on a Honeywell 14-Channel tape recorder, type LAR 7470/7490, made available by NASA-Ames Research Center. This recording technique also permitted convenient data reduction by the Bell Data Acquisition Laboratory.

The time restrictions imposed on each program being performed in a large scale wind tunnel made a second measuring system as a back-up system necessary, enabling the test team to monitor and read the significant test data from instruments during each run and evaluate the quality of the tape-recorded data. This back-up system proved to be very useful; preliminary evaluations and decisions as to required program changes were obtained within a short time.

A block diagram of the monitoring and recording systems is shown in Figure 3. The output signal of each of the six microphones is fed to a microphone amplifier and through a normalizing attenuator to a precision vacuum tube voltmeter for reading rms-sound pressure levels. The same output could also be displayed on either an oscilloscope or on a panoramic analyzer. Selected displays were photographed with a Polaroid Land camera. Also, a narrow band analysis could be conducted during the test if desired. The same three instruments served for quality control of the tape records during playback. Two other channels of the tape recorder recorded the output of an accelerometer and a microphone position indicator. An instrumentation set up is shown in the photo Figure 4.

4. Calibration

An acoustical calibration of each microphone channel was performed on the beginning of the tests and at certain intervals during the program with a B.a.K piston-phone. This method gives an output sensitivity of the entire circuit in relation to a calibrated sound pressure produced in the pistonphone cylinder at a driving frequency of 250 cps. However, the acoustic calibration is restricted to a sound pressure level of 124 db (rms). To cover the dynamic range of interest (up to 170 db) and to check the linearity of the entire circuit including amplifiers, an electric calibration had to be conducted prior to and after each run. It was also tape recorded. This calibration is obtained by injecting a known A-C signal from a signal generator into the microphone charge amplifier. This signal can be made to be equivalent to the microphone output due to a sound pressure level. The same method was applied to calibrating the accelerometer circuitry.

C. PROPULSION INSTRUMENTATION

As shown in Section II, the sound field inside the duct may be calculated if the three propeller quantities, propeller thrust T_p , torque Q and rotational speed N are known. The

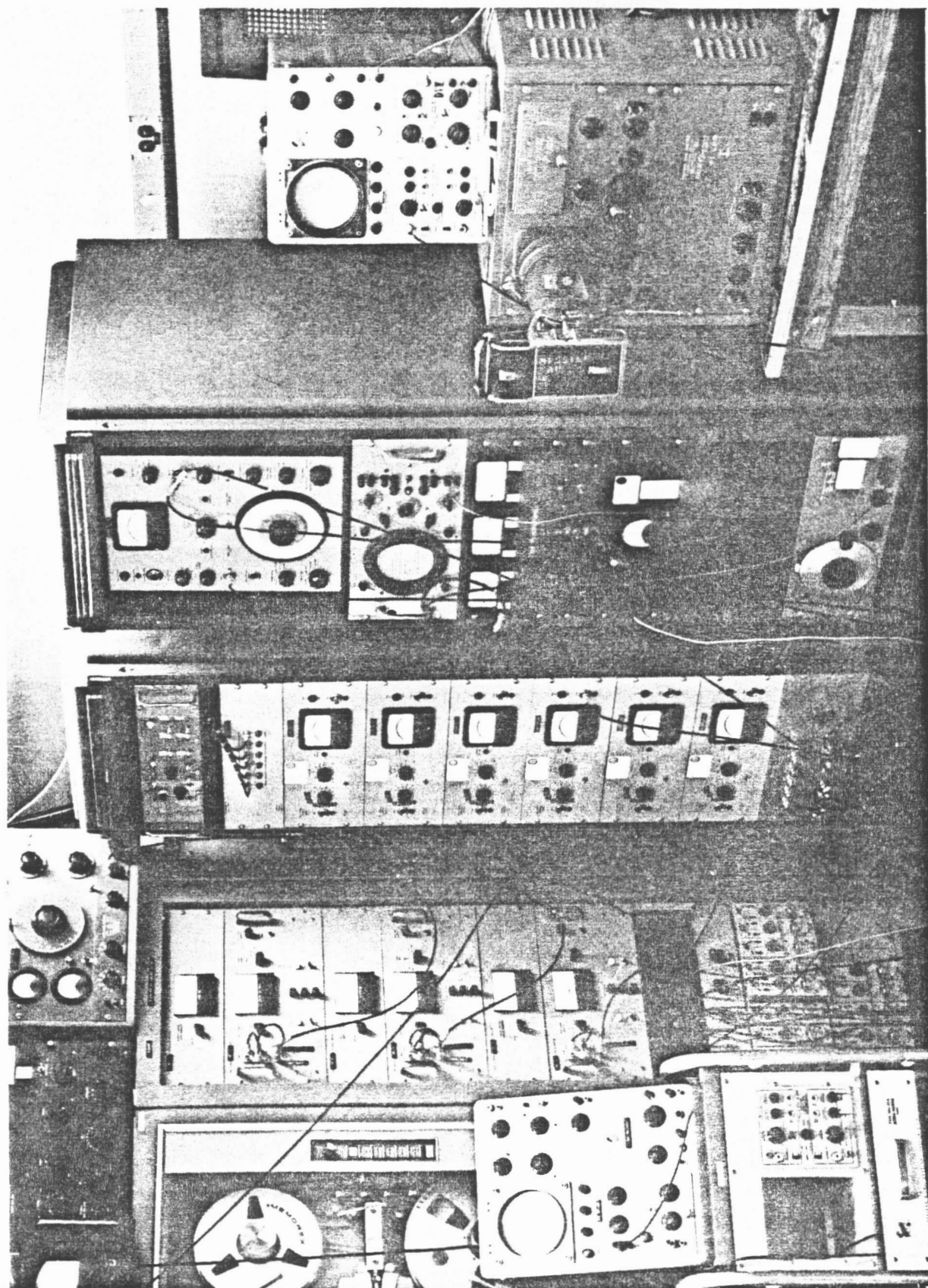


Figure 4. Instrumentation Setup

following section presents a brief description of the propeller test stand installed inside the 40 x 80 ft wind tunnel and of the associated propulsion instrumentation prepared by NASA-Ames Research Center for measuring these three quantities.

The model is pylon-mounted above a ground board, the pylon extending through the duct (with no contact) and supporting the entire model by its centerbody (Figure 5). The pylon is enclosed from the duct to the centerbody by the power strut fairing, and between duct and ground board by an air foil section representing a wing from the engine nacelles to the duct. This section is mounted to the ground board and is free of contact with the model.

The propeller is powered by a 1500 horsepower, three-phase induction motor, installed vertically beneath the ground board. Power is transmitted by a vertical shaft through a right angle gearbox in the centerbody (Figure 6). The motor speed can be changed over a wide range by a variable-frequency motor-generator. A watt-meter monitors the motor input power.

Attaching the motor support to the tunnel scale balance (without any contact to the wing fairing and ground board) permits sensing the forces and moments of the entire model.

The thrust of a ducted propeller is the difference between the total thrust and the duct thrust and may be obtained by measuring these two quantities individually. Based on this principle, a thrust measuring method is under development by NASA-Ames Research Center. For total thrust measurements, the wind tunnel scale is used. Duct thrust is measured by two strain-gaged load cells, attached to the two ends of the main beam supporting the duct. It became apparent during the course of the test program that this device, still in the developmental state, did not allow accurate measurements because zero readings could not be repeated. At increased propeller power, one load cell broke, and it was decided to install locking plates over both load cells. This arrangement permitted a continuation of the tests without redesigning the load cells that would have caused an intolerable rescheduling of the wind tunnel program. Of course, the separate measurement of both thrust values as planned at the beginning of the program was excluded.



Figure 5. Scale Model on Tunnel Floor

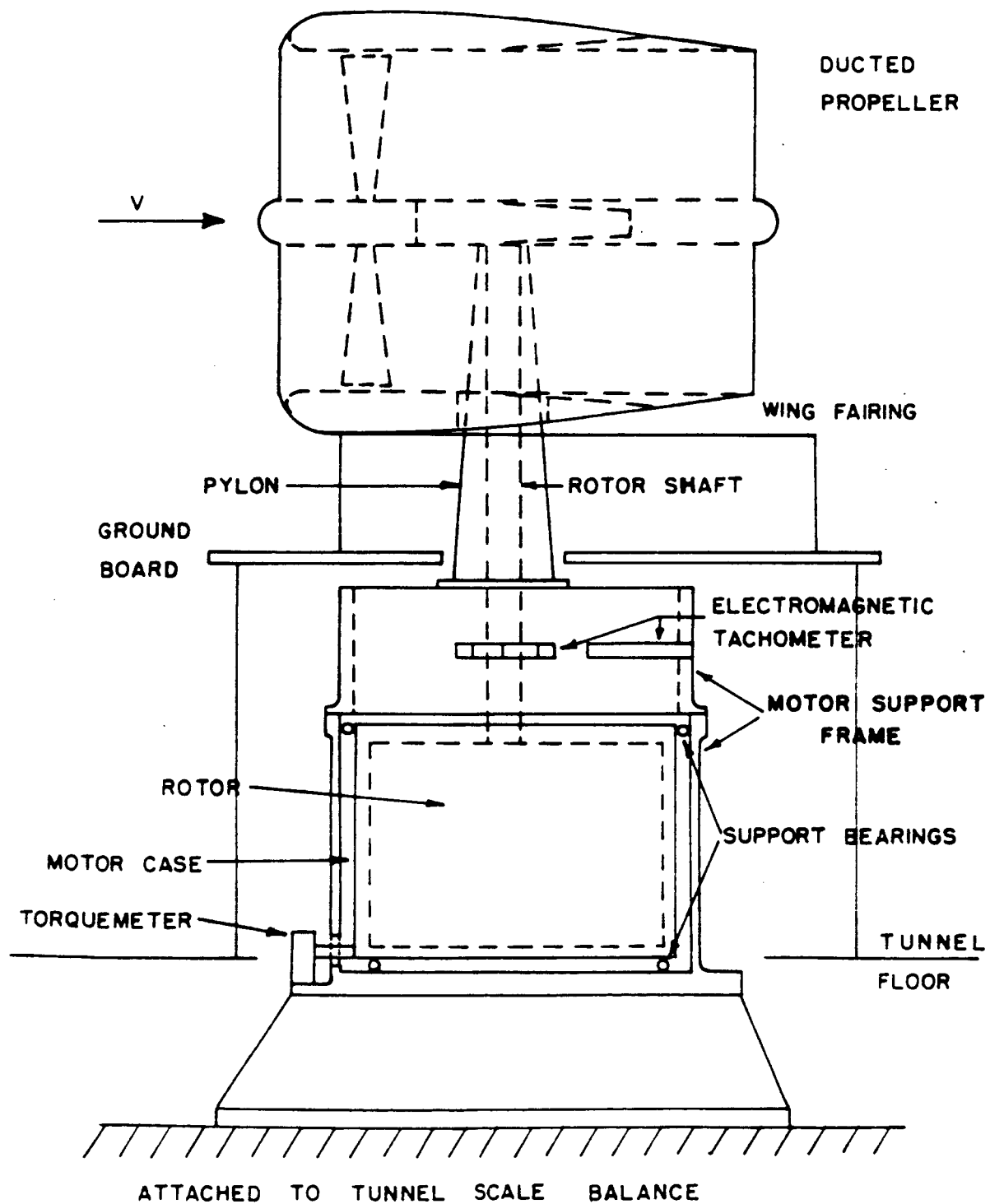


Figure 6. Schematic of Motor Suspension for Measuring Propeller Thrust and Torque

NOT TO SCALE

An alternate method for determining the propeller thrust had to be selected. This quantity was calculated from the measured total thrust. The computation used the simple momentum theory, which states that the division of the total thrust between the propeller and duct may be expressed by

$$\frac{T_D}{T_P} = 2 \frac{A_c}{A_p} - 1$$

where T_D = duct thrust

T_P = propeller thrust

A_c = exit plane area

A_p = propeller plane area

The propeller-thrust is then obtained from the total thrust T_T

$$\text{where } T_P = \frac{1}{2} T_T \frac{A_p}{A_c}$$

$$T_T = T_P + T_D$$

These expressions apply only for the static case.

The second important quantity, propeller torque, was measured by a strain-gaged torquemeter. This device consists of a load cell mounted to a two-foot long arm. The load cell measures the reaction force between the motor support frame and the motor case which was supported on bearings. Under the assumption of negligible friction losses in the transmission system including gearbox, the torquemeter reading indicates the propeller torque.

An electromagnetic tachometer was applied for measuring the rotational speed N . It consisted of a 60-tooth gear attached to the motor shaft, and a magnetic coil mounted to the motor frame. The signals produced by the variation of the magnetic resistance are fed to an electronic counter.

From the two measured quantities torque Q and rotational speed N , the propeller power P is calculated

$$P = 2\pi NQ$$

D. TEST PROGRAM

As discussed in the introduction, the main objective of the tests was to validate analytical expressions which relate the sound pressure inside the duct to the three quantities: propeller torque, propeller thrust, and rotational speed. Accordingly, a test program was prepared to obtain measurements and tape records of the sound pressure at all six microphone positions for a wide range of propeller blade angles from 17° to 41° and a propeller rotational speed from 500 to 2200 rpm. The resulting values of total thrust and propeller thrust varied up to 3000 lb and 1500 lb respectively. Maximum power supplied to the propeller shaft was 780 hp, the limit being the tolerable dynamic load on the duct.

The overall sound pressures were monitored at the beginning of each run by an oscilloscope, vacuum tube voltmeter and panoramic analyzer to assure that the values did not exceed the dynamic range of the microphone circuit and to obtain preliminary data of the pressure-time function, wave form and number of harmonics. During selected runs, photographs of displays of the oscilloscope and panoramic analyzer were taken.

The next step, following this survey, was the electric signal calibration, recorded on tape, with subsequent tape recording of all six sound pressure values and also of certain acceleration data. Finally, the record was played back and monitored by the same instruments as used for the survey.

All measurements related to the main objective of the study were conducted with the six microphones in a position flush with the inner duct surface under static conditions (without operating the wind tunnel) at a constant tip clearance of $3/8$ inches. For the last run, at the end of the program, the tip clearance was changed to 1.5 inches to obtain experimental data useful for defining the significance of tip clearance with respect to the duct sound field.

Two runs were conducted under dynamic conditions at a wind tunnel speed of 171 ft/sec.

A modification of the spinner made during the course of the contract by the propeller manufacturer as part of another NASA-sponsored contract, as well as the reduced wind tunnel test time, restricted the radial exploration to one plane aft of the propeller. The two other movable microphones remained in a position flush with the duct surface during all tests.

IV. RESULTS OF EXPERIMENTS

A. INTRODUCTION

This section presents a detailed discussion of all test results, beginning with a description of typical recorded sound pressure-time functions, followed by an interpretation of selected spectra obtained by a harmonic analysis. Also, the measured effect of tip clearance on sound pressure and the result of a radial exploration of the duct sound field will be discussed.

B. RECORDED SOUND PRESSURE-TIME FUNCTIONS

For a survey of the true sound pressure time function, the tape recorded signals were reproduced and recorded on a pen recorder, type Brush Mark 200, to compare the wave forms existing at different positions of the duct wall. A typical excerpt of sound pressure-time functions, measured by all six microphones at two different rotational speeds, is shown in Figures 7 and 8. The individual pressure pulses, resulting from the aerodynamic pressure pattern rotating with the blades, are clearly indicated. The time interval, measured between each pulse, is the blade passage time and is in agreement with the value calculated from the rotational speed and number of blades. The figure demonstrates (within the frequency response limitations inherent in a pen-recorder) the different character of waves between the two microphone groups located either in front or aft of the propeller plane. The outputs of the first three microphones (lower three traces) are periodic functions; the wave form repeats at each blade passage. However, aft of the propeller plane, the sound pressure-time function appears to become more random as demonstrated by the upper three traces. Microphone No. 4 still indicates periodic pulses superimposed over a random function. But, the wave forms of the last two microphones No. 5 and No. 6 are of random character,

More details in the wave form recorded by the first three microphones were obtained by reproducing the tape recorded data on an oscillograph as shown in Figures 9

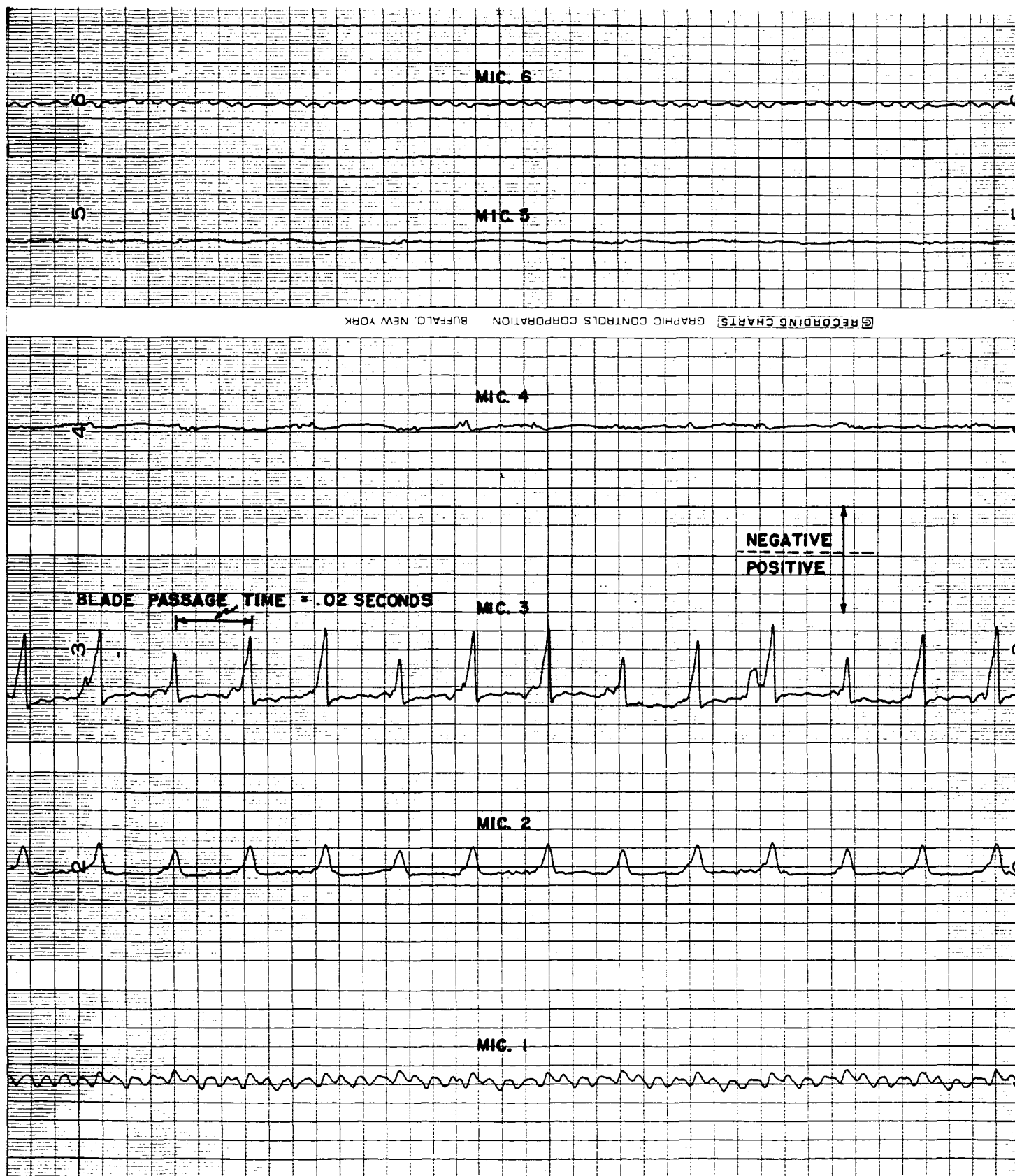


Figure 7. Sound Pressure-Time Function (Run No. 8, $N=1000$ rpm $\beta = 17^\circ$)

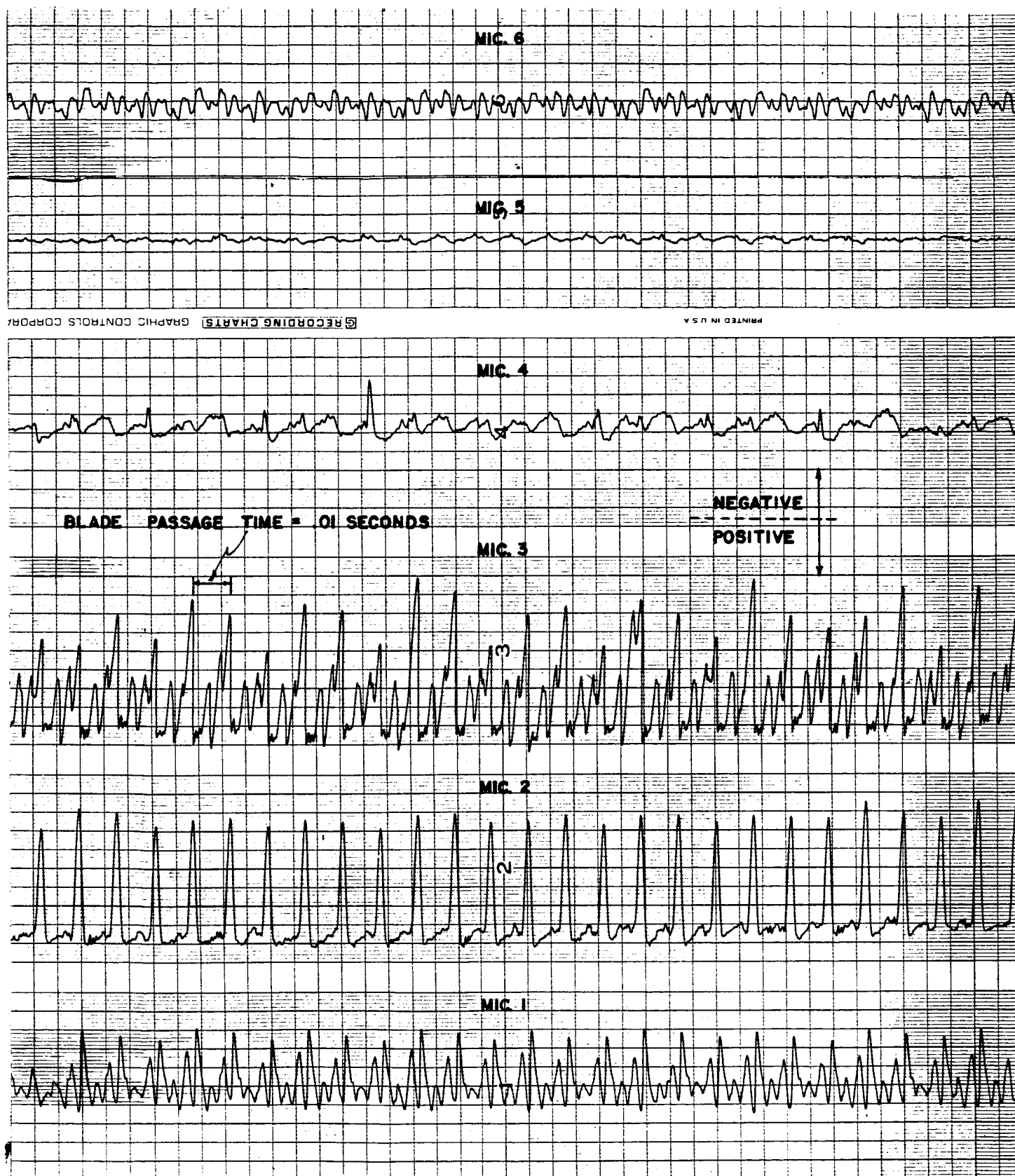


Figure 8. Sound Pressure-Time Function (Run No. 8, $N = 2000$ rpm, $\beta = 17^\circ$)

and 10 for the same run No. 8 at two rotational speeds. These figures show an increase of the number of harmonics sensed by microphone No. 3 in the propeller plane, with increased tip speed. Typical of all oscillograms is a modulation of the sound pressure peaks, repeating at every propeller shaft revolution. This effect predominates in the propeller plane, where the ratio of maximum to minimum peak sound pressure can reach a value of two at $N = 2400$ rpm. It may be explained by a tip clearance variation, caused by a relative motion between duct and centerbody.

In connection with this result, it is interesting to discuss the acceleration of the duct due to mechanical vibration. During the first runs, the vertical duct acceleration was recorded at two different points, using quartz-accelerometers mounted inside the duct structure. One accelerometer was located in front of the propeller plane, the other one close to the trailing edge near microphone 6. The results showed that the acceleration increases with increased distance from the propeller plane towards the trailing edge. Consequently, during the subsequent tests, the trailing edge was selected as the most sensitive area for monitoring the duct acceleration.

An evaluation of the overall acceleration of the duct recorded at the trailing edge showed an increase of this value with the rotational speed. Parallel to this increase, the energy of the acceleration spectrum shifts as demonstrated in the acceleration spectra Figures 11 and 12. At $N = 1500$ rpm, the first peak of the spectrum is the blade passage frequency. An increase of N to 2400 rpm results in a change of the acceleration spectrum. The first peak appears now at the propeller shaft frequency. The last result justifies the assumption that the modulation of the sound pressure peaks recorded at high rotational speed is the result of a variation of the propeller tip clearance due to the relative motion between propeller and duct.

The acceleration test results discussed above can also be evaluated to determine the undesired microphone signals caused by mechanical vibration and superimposed over the output signal due to the sound pressure. This error analysis, of course, could only be conducted for the output of microphone No. 6, located at the trailing edge, where the sound pressure is low, but where the duct acceleration reaches its maximum. Consequently, the result is considered to be conservative.

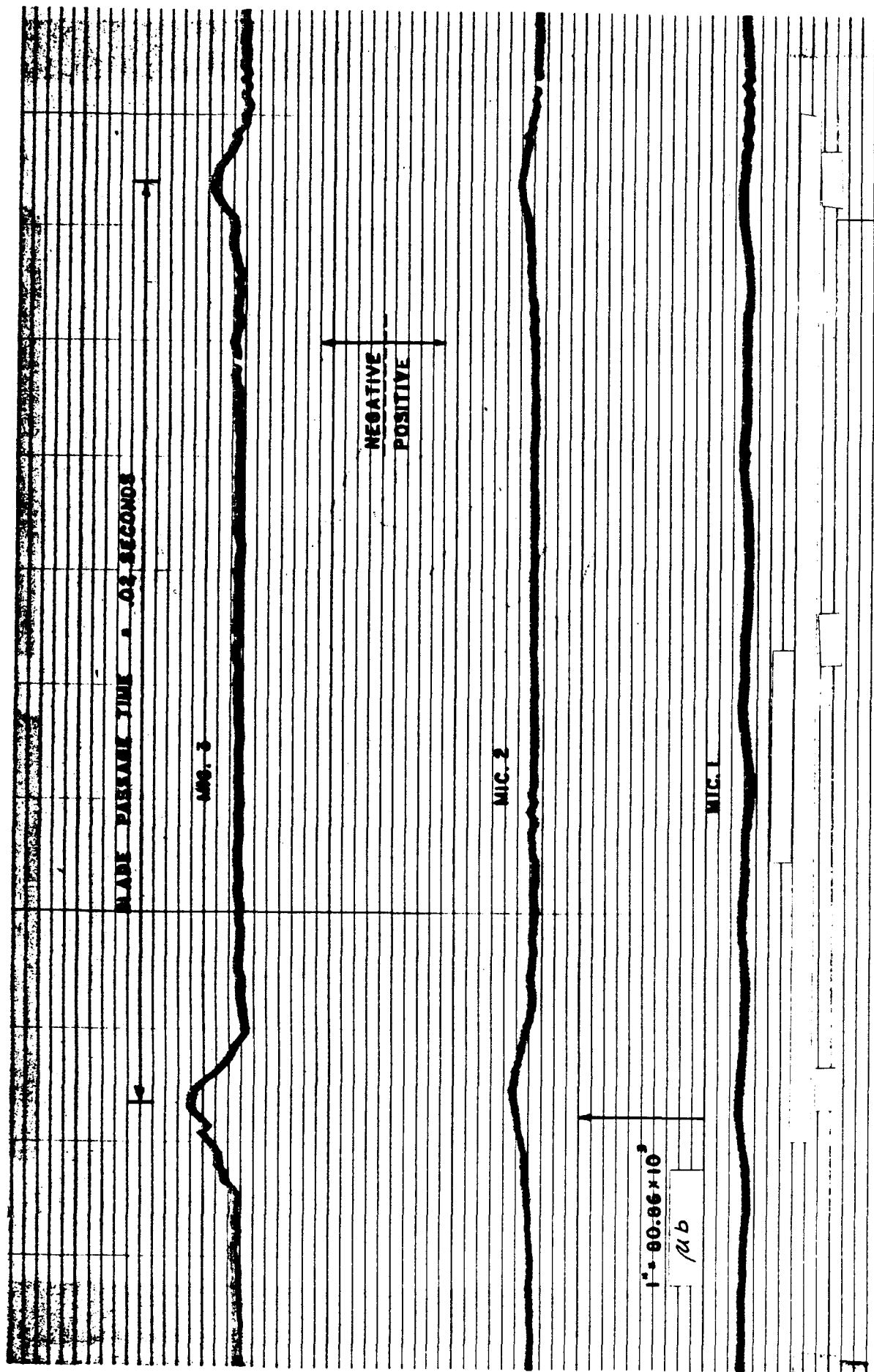


Figure 9. Sound Pressure-Time Function (Run No. 8, $N = 1000$ rpm, $\beta = 17^\circ$)

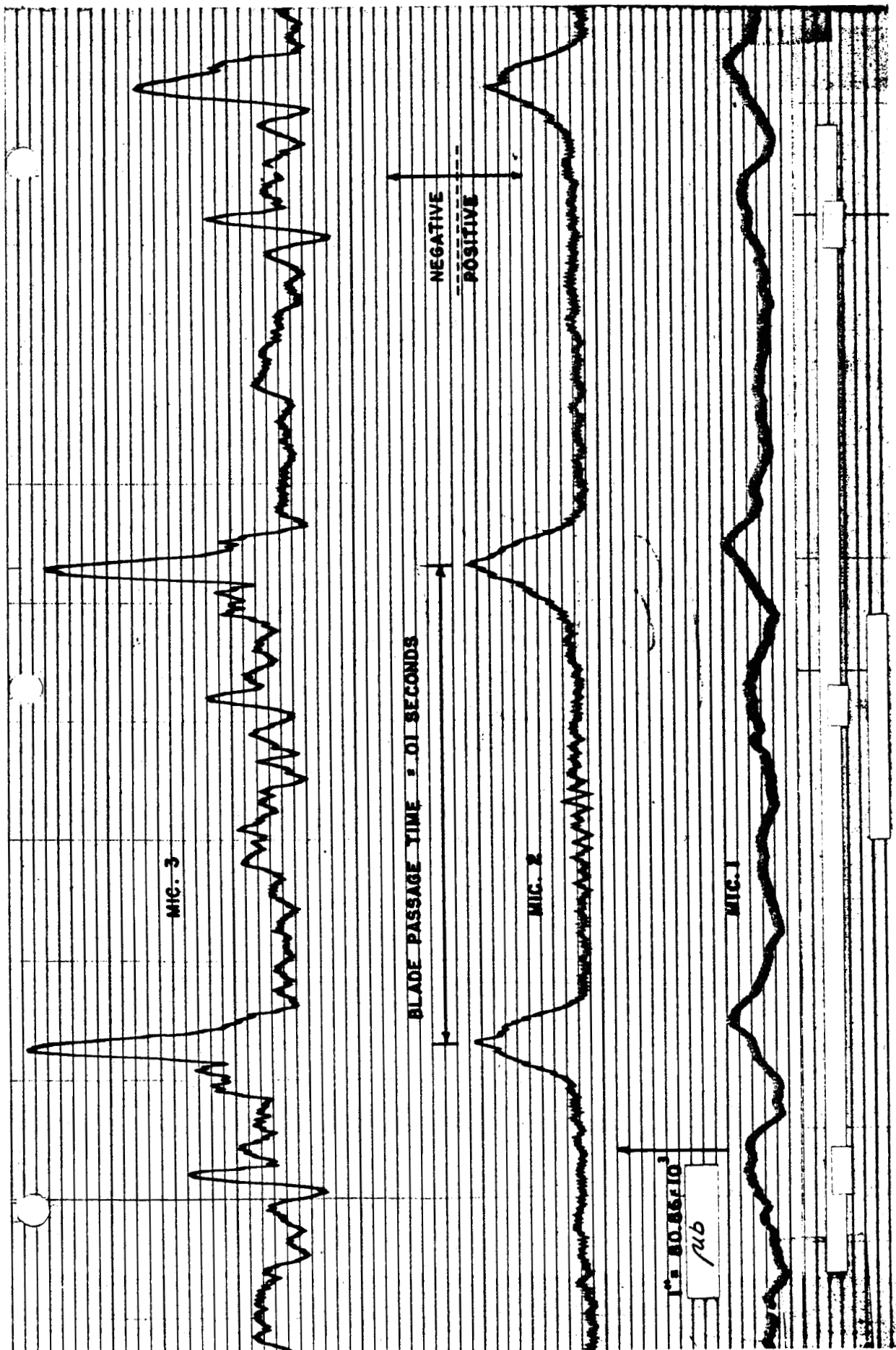


Figure 10. Sound Pressure-Time Function (Run No. 8, $N = 2000$ rpm, $\beta = 17^\circ$)

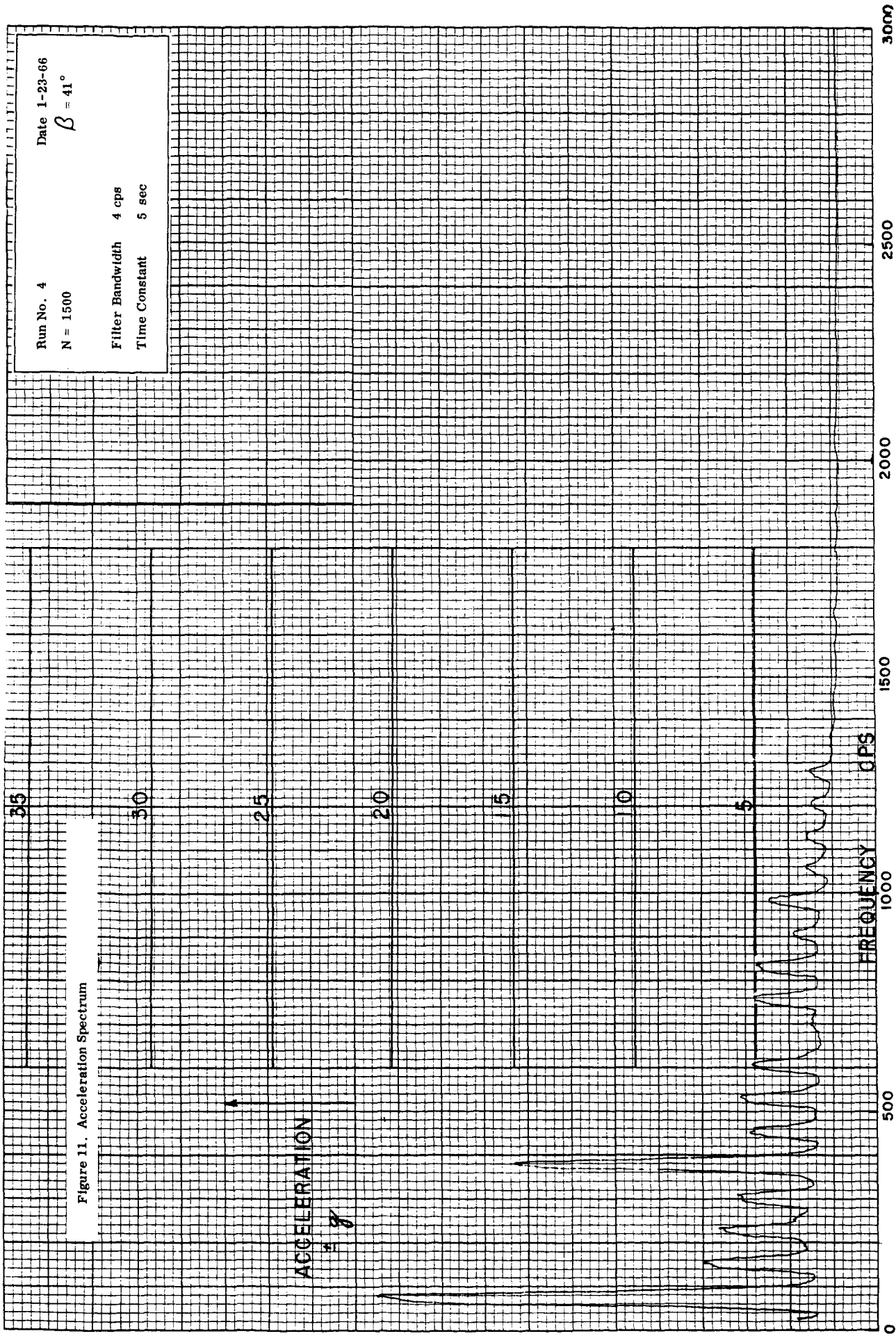


Figure 12. Acceleration Spectrum

Run No. 8
 Date 1-27-66
 $\beta = 17^\circ$

N = 2400 rpm

Filter Bandwidth 4 cps

Time Constant 0.5 sec

FIRST THREE HARMONICS OF
 SHAFT FREQUENCY

ACCELERATION
 $\pm g$

FREQUENCY CPS

0 500 1000 1500 2000 2500 3000

The vibration sensitivity of the quartz accelerometer used for these measurements was 88 db/1 g rms. The rms-acceleration recorded on tape for a number of runs varied from 2 to 20 g, depending on blade angle and rotational speed. These acceleration values would have resulted in microphone outputs between 94 and 114 db. The recorded sound pressure levels ranged from 130 to 150 db. It can be seen that the differences between both outputs always exceed 30 db. At that difference, the error of the sound pressure measurement is less than 0.1 db and, therefore, negligible.

Decreasing the attenuation in the tape recording circuit of Figure 3 or increasing the gain of the oscillograph circuit permitted a variation of the scale factor of the oscillograms to any desired value, in particular for the outputs of the three microphones No. 4, 5, and 6. For comparing and for an evaluation of all six sound pressure-time functions, the oscillogram obtained from run No. 8 was normalized and redrawn as presented in Figure 13. Of particular interest is the fact that the ratio of peak-to-peak to rms value of the sound pressure may be as high as 7 in the propeller plane. (For a sinusoidal wave, this ratio is 2.83.) The increase in this ratio has to be considered for a prediction of the acoustic fatigue life of duct structures.

C. HARMONIC ANALYSIS

A harmonic analysis, performed with a wave analyzer: (Technical Products Company, TP-625), supported the conclusions made in the previous section. Using the same scale factor for sound pressure, the relative peak values of the harmonics were plotted versus frequency. They are presented for run No. 8 in Figures 14 and 15 for the two microphones No. 2 and No. 3. Each plot compares the spectra at the two rotational speeds $N = 1000$ rpm and 2400 rpm. At low speed, the amplitudes of the harmonics decay more rapidly than those at high speed. At the propeller plane, the spectra show an increase of the number of higher harmonics. The spectrum at $N = 2400$ rpm reveals the existence of more than 25 harmonics.

Also confirmed by the harmonic analysis is the more or less random type of spectra for the second group of microphones located aft of the propeller plane. Typical is the spectrum sensed by microphone No. 5 and shown in Figure 16. Only a few of the peak amplitudes in this spectrum can be identified as harmonics of the blade passage frequency.

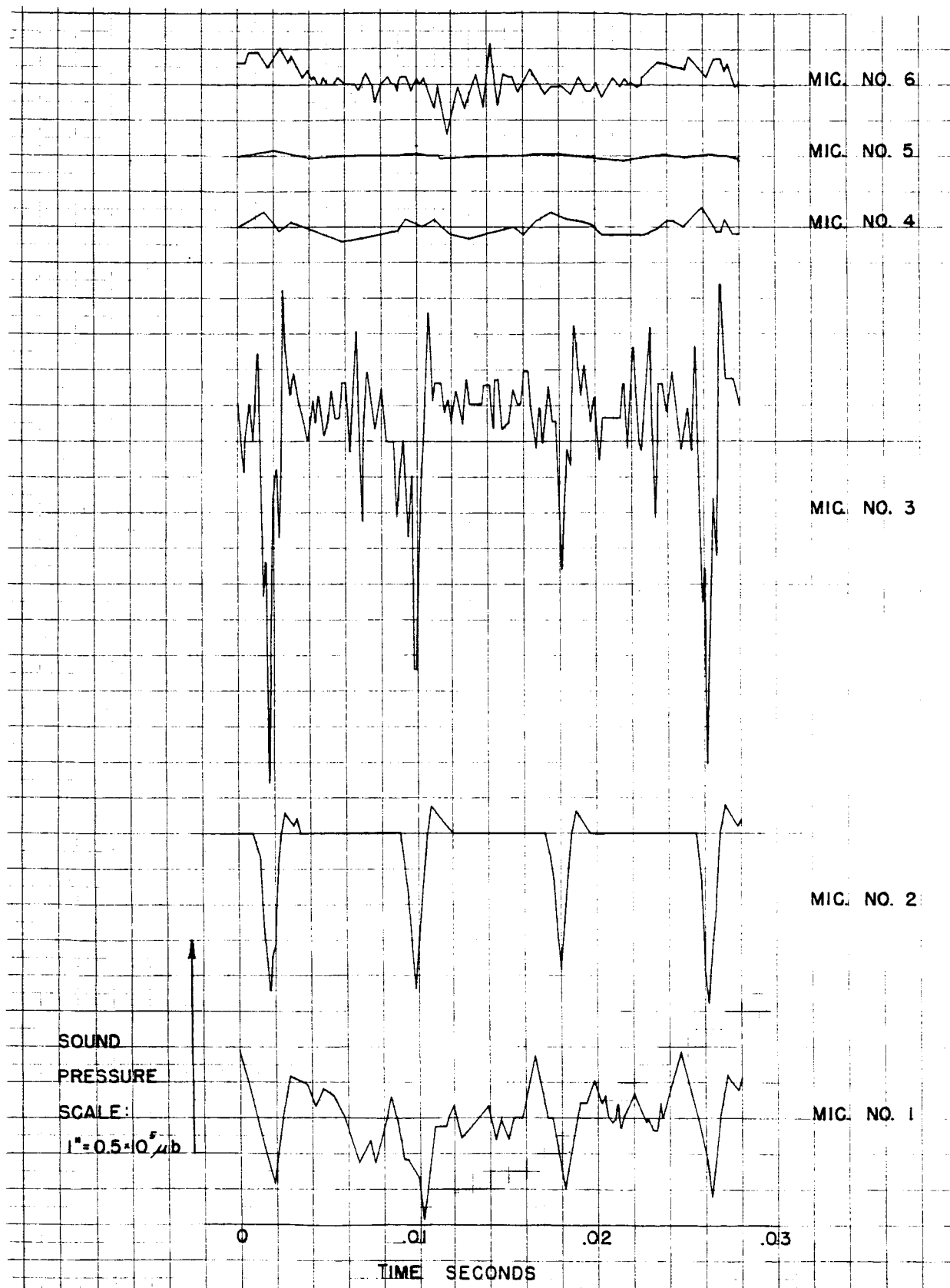
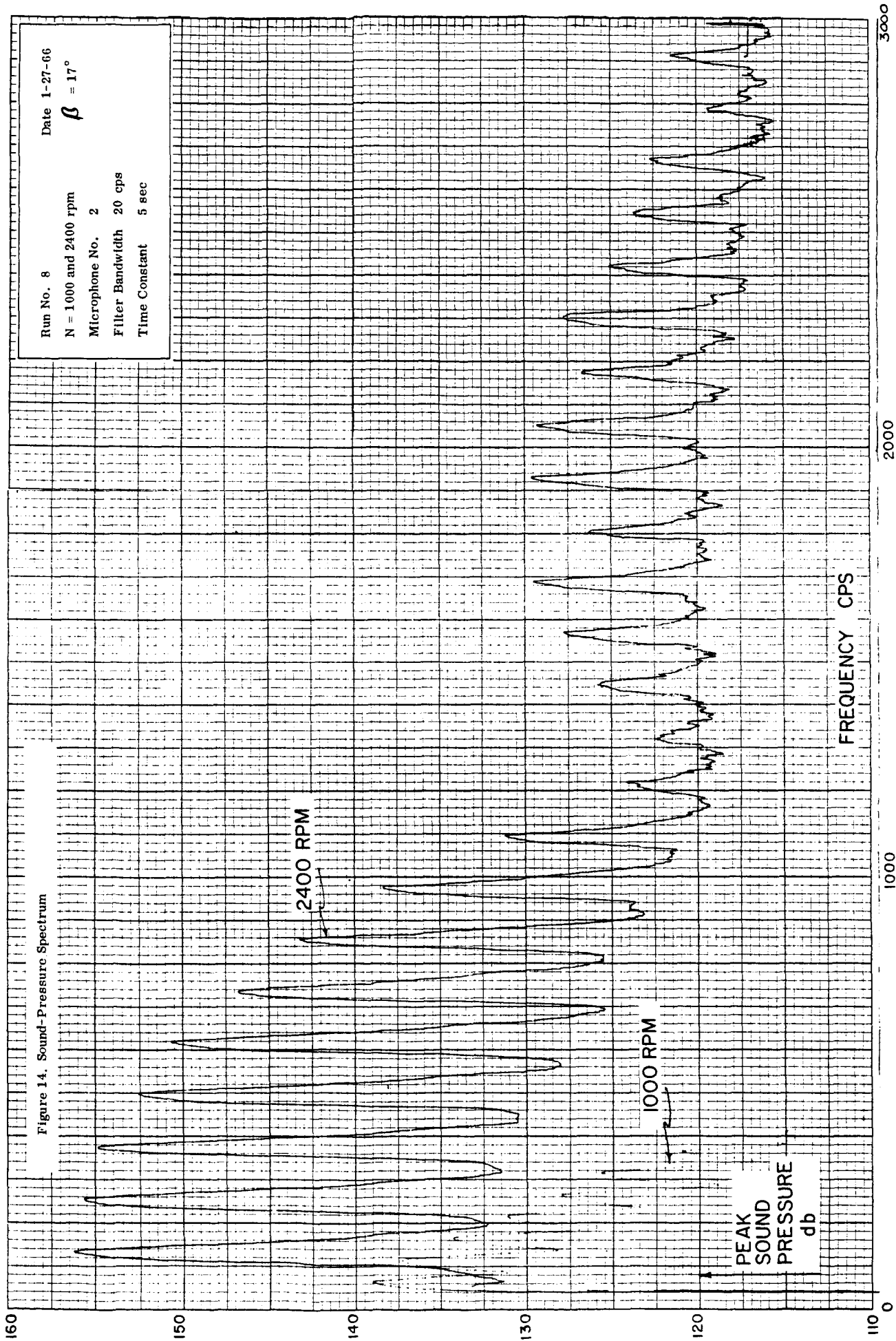
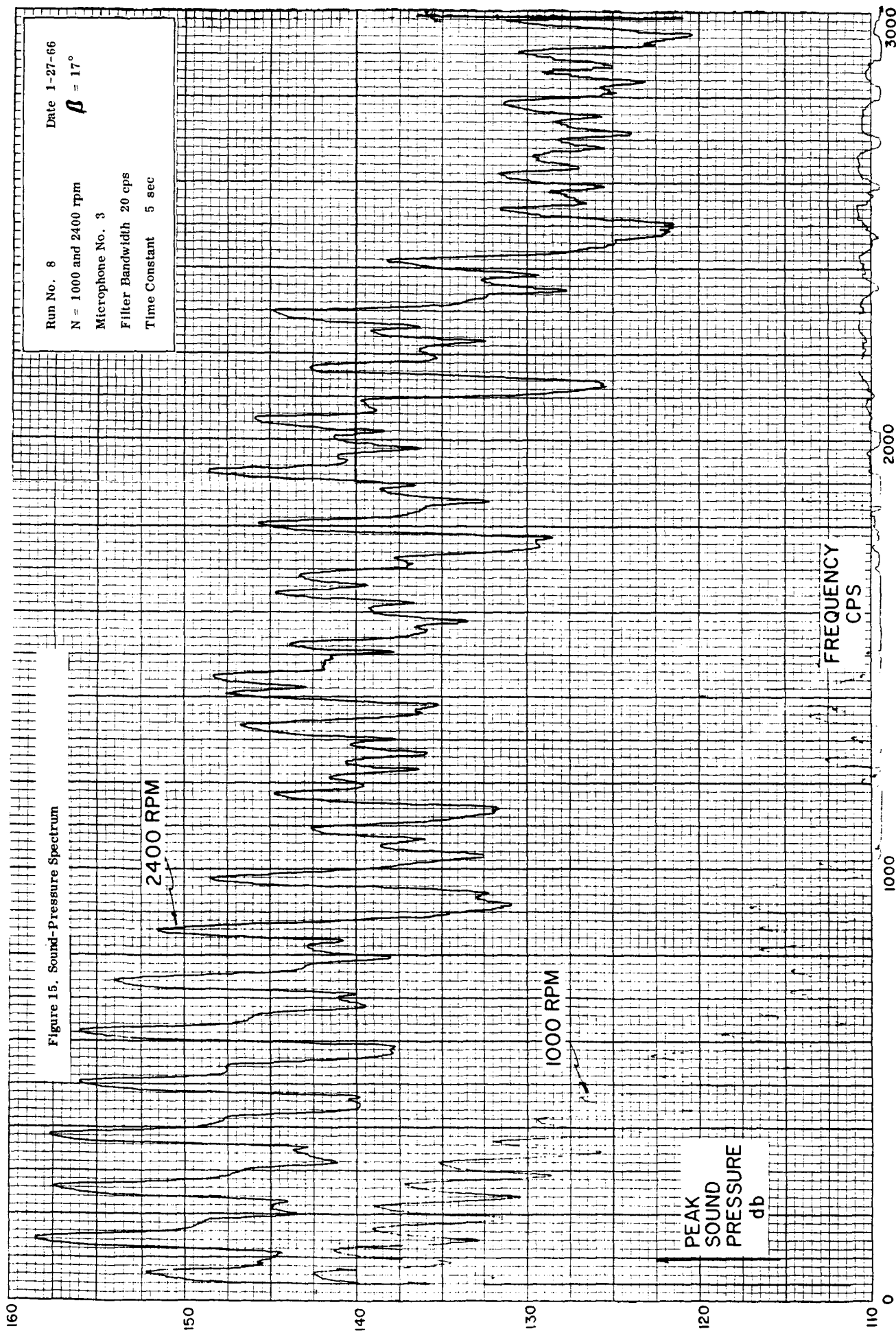


Figure 13. Recorded and Normalized Sound Pressure-Time Functions at Six Microphone Positions (Run No. 8, N = 2400 rpm)





160

Run No. 8

Date 1-27-66

N = 2400 rpm

 $\beta = 17^\circ$

Microphone No. 5

Filter Bandwidth 20 cps

Time Constant 5 sec

150

140

Figure 16. Sound-Pressure Spectrum

130

120

PEAK
SOUND
PRESSURE
dB

FREQUENCY ~ CPS

110

500

1000

An examination of the other test runs indicated the same spectral change. No final conclusion can be made at the present time. However, the assumption is justified that the change from a periodic to a random spectrum may be attributed to the generation of a random pressure field due to turbulence from the propeller blades, that is superimposed over the periodic pressure pulses.

D. EFFECT OF TIP CLEARANCE ON SOUND PRESSURE

Since the analytical approach presented in Section II of this report does not consider a finite tip clearance, one test was conducted at a tip clearance of 1.5 inches in order to ascertain the significance of tip clearance on the sound pressure field.

An increase of the tip clearance from 3/8 to 1.5 inches resulted in a reduction of the overall sound pressure level as shown in Figure 17. For this plot, data of Runs No. 6, 11, and 12 were used⁽¹⁾. All three tests were conducted under the same operational conditions (propeller blade angle of 23°), with test No. 11 at the large tip clearance. The tape recorded overall sound pressure levels sensed in tests No. 11 and 12 along the duct in front of the propeller plane were extrapolated to the propeller plane.

The different wave forms obtained at two tip clearances can be well recognized by comparing the sound pressure time functions sensed in front of the propeller plane (microphone No. 2) as shown in Figures 18 and 19. At small tip clearance, the sound pressure peak is approximately twice as high as that at large tip clearance, and the pulse width is reduced. The results of an evaluation of the peak-to-peak sound pressures, expressed in decibels, are shown in Figure 20. It indicates the same differences of sound pressure levels due to tip clearance variation as obtained for the overall sound pressure levels.

⁽¹⁾ At the beginning of test No. 11, three of the microphone cables from the recorder room to the model became disconnected. The time made available to this test phase did not permit a search for the location of disconnection. Consequently, only the remaining 3 microphones could be used for test No. 11 and 12.

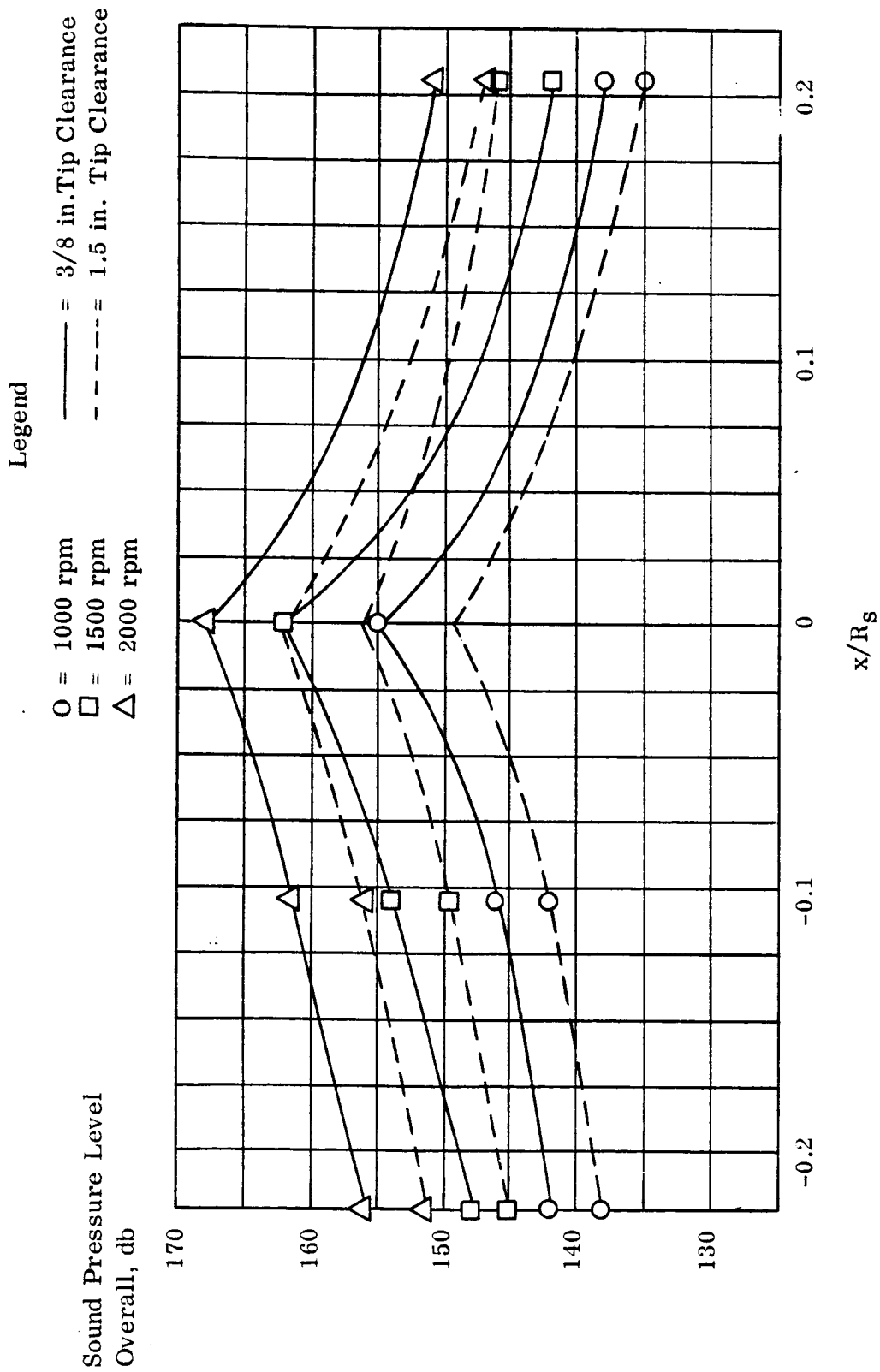


Figure 17. Effect of Tip Clearance on Overall Sound Pressure (Data from Runs 6, 11, and 12)

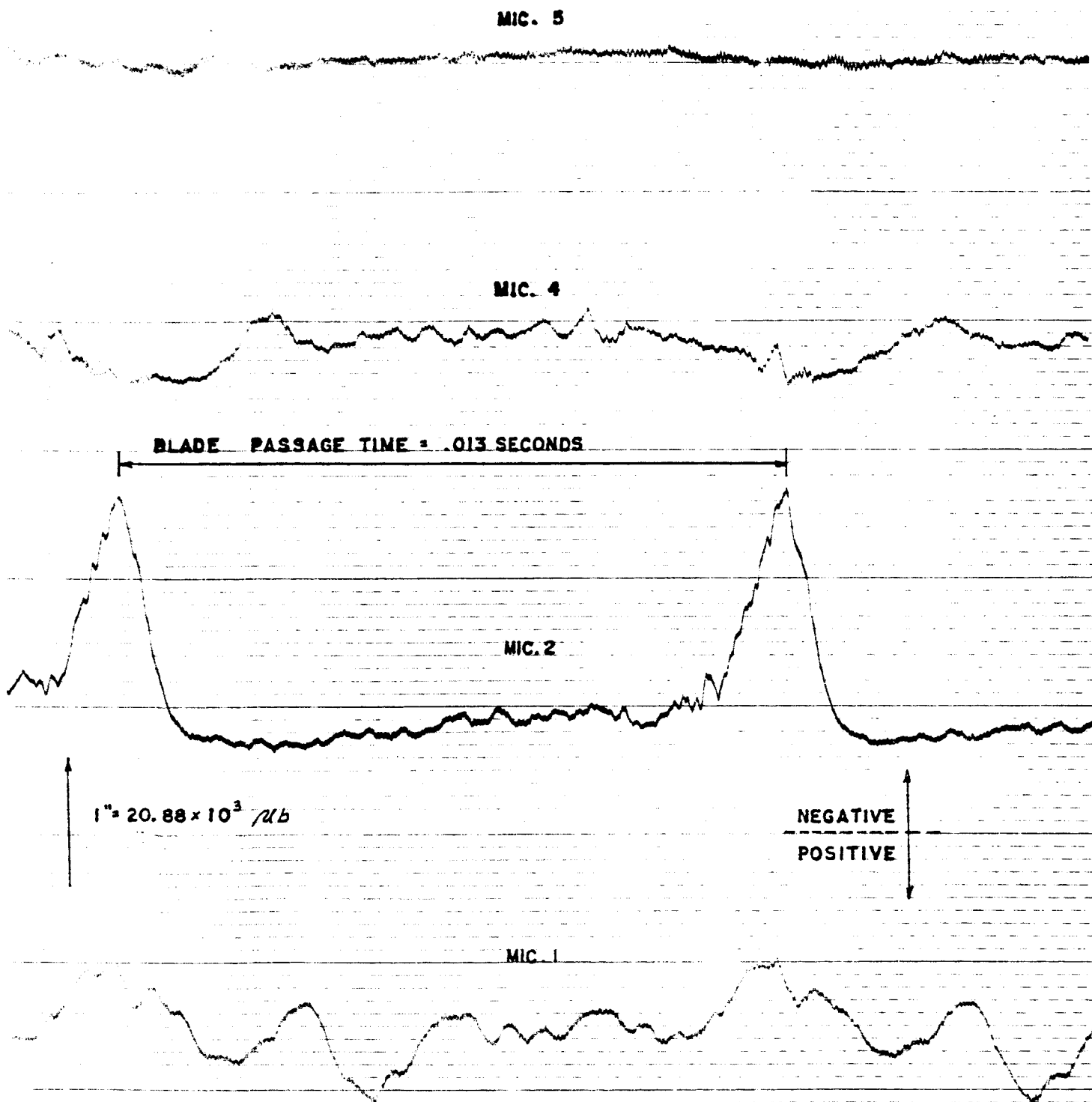


Figure 18. Sound Pressure-Time Function
(Run No. 12, $\Delta R = 3/8$ in., $N = 1500$ rpm, $\beta = 23^\circ$)

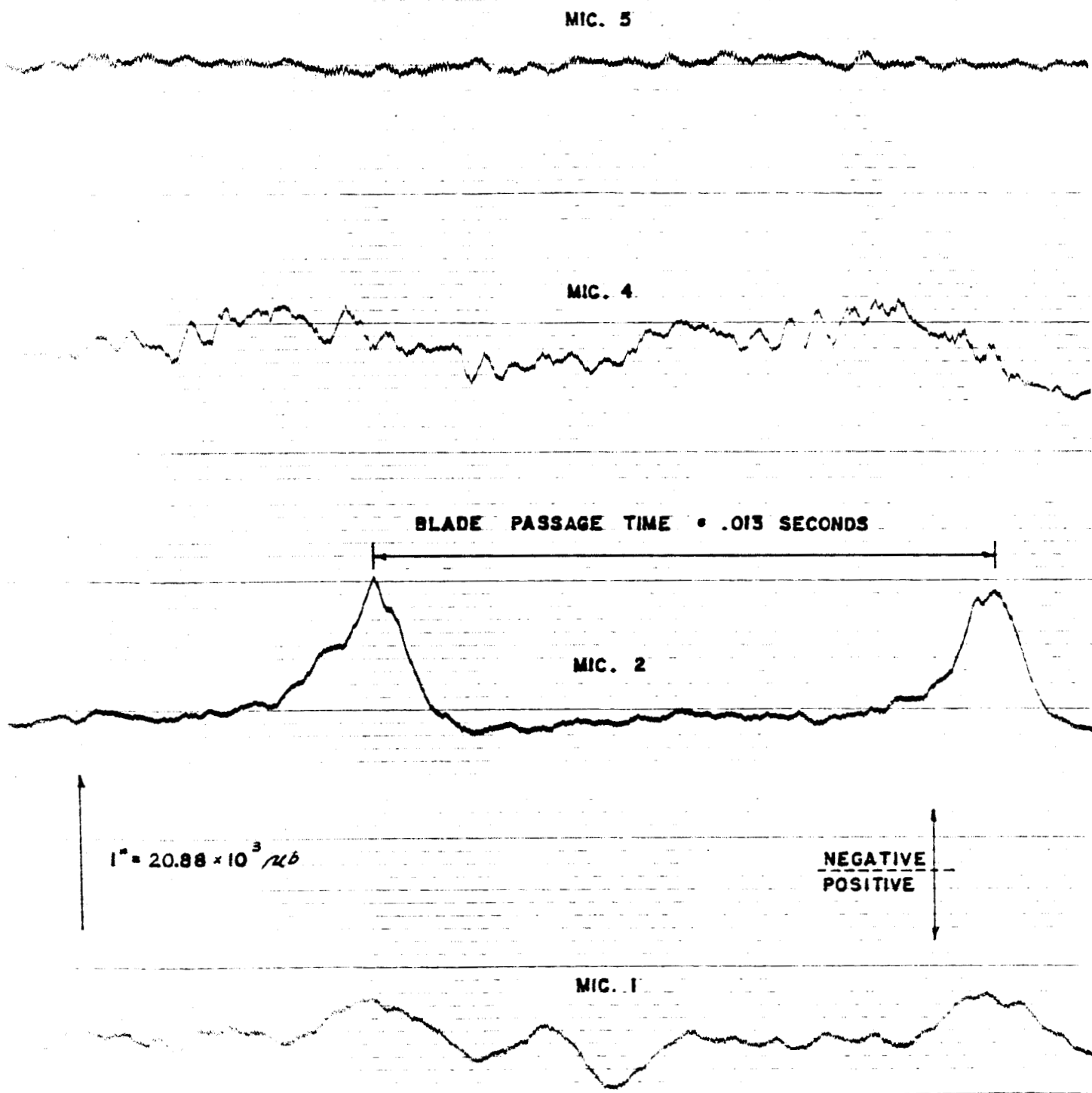


Figure 19. Sound Pressure-Time Function
(Run No. 11, $\Delta R = 1.5$ in., $N = 1500$ rpm, $\beta = 23^\circ$)

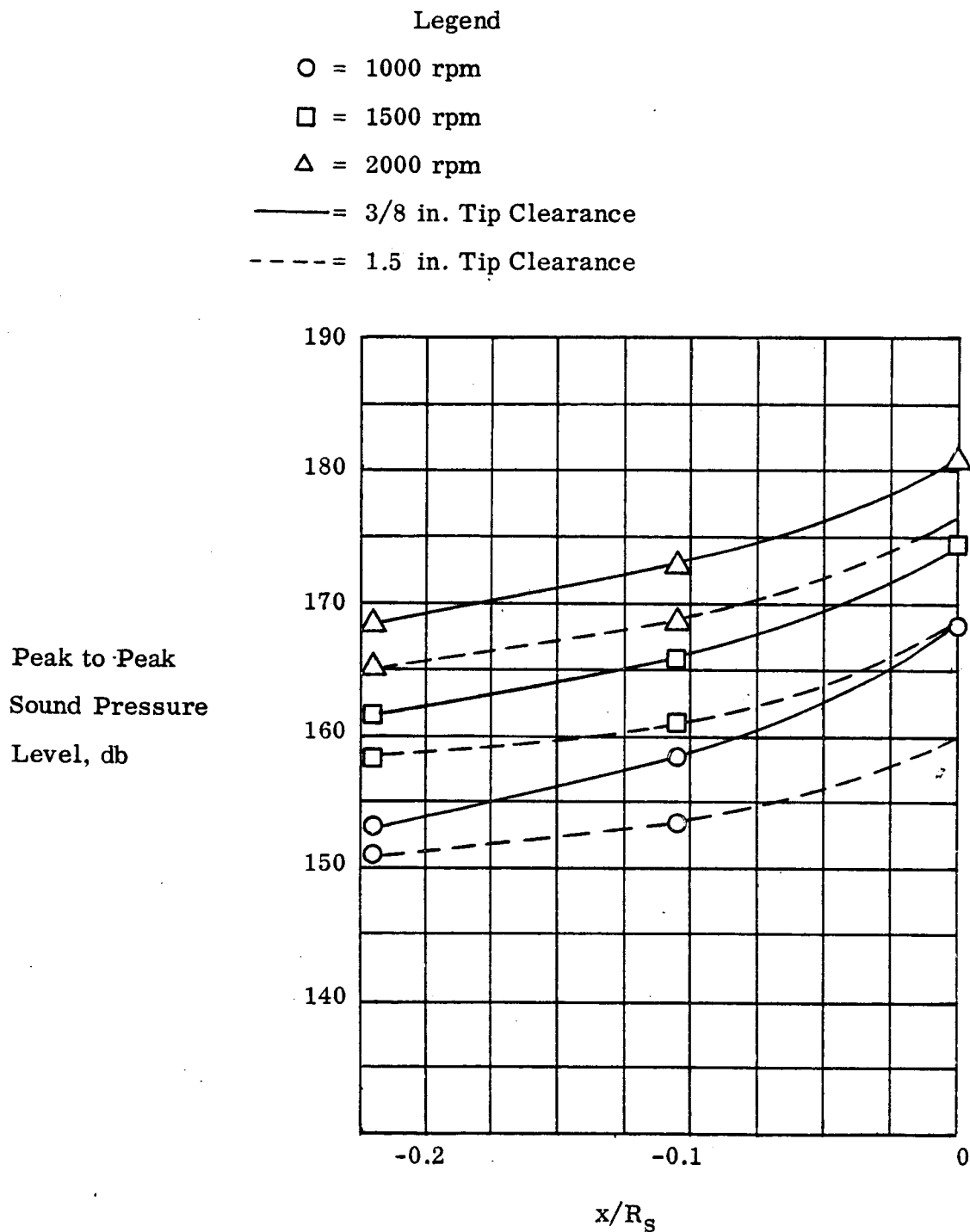


Figure 20. Effect of Tip Clearance on Peak to Peak Sound Pressure,
(Data from Runs 6, 11, and 12)

E. RADIAL SOUND PRESSURE FIELD, TEST RESULTS

As mentioned in Section III.D, the radial exploration of the sound pressure field was conducted during run No. 15 by traversing the duct behind the propeller plane from the inner duct wall to the hub surface, using microphone No. 5. The overall sound pressure levels and also the radial microphone positions were tape recorded and later reproduced on a X-Y recorder, type Electro-Instrument. Figures 21 and 22 show the overall sound pressure level versus travelled distance at two rotational speeds $N = 1500$ rpm and $N = 2000$ rpm. The zero point of the X-Y record indicates the flush position of the microphone. The overall sound pressure decreases with increasing radial distance from the duct wall, but increases, after approximately 12 inches of travel, by 10 db close to the hub surface.

To facilitate the explanation of these unexpected results, a harmonic analysis of the sound pressure measured at three different microphone positions was conducted. The resulting spectra are presented in Figures 23, 24, and 25. Within the region close to the duct wall, the spectrum resembles that measured at the same duct location by the flush-mounted microphone. Periodic pressure pulses exist only at low frequencies identified as harmonics of the blade passage frequency (Figure 23). The number of harmonics decreases if the distance from the duct increases (Figure 24). Close to the hub surface, the spectrum becomes completely random as demonstrated in Figure 25.

During this test, a flow velocity survey was made across the duct section. This indicated that the propeller blades were stalled in this region over the first nine inches from the hub. The turbulent wake resulting from this condition could well be the source of the random noise indicated by the spectral analysis recorded in Figure 25. The effect of turbulence on the radial sound pressure distribution will be further discussed in Section V.

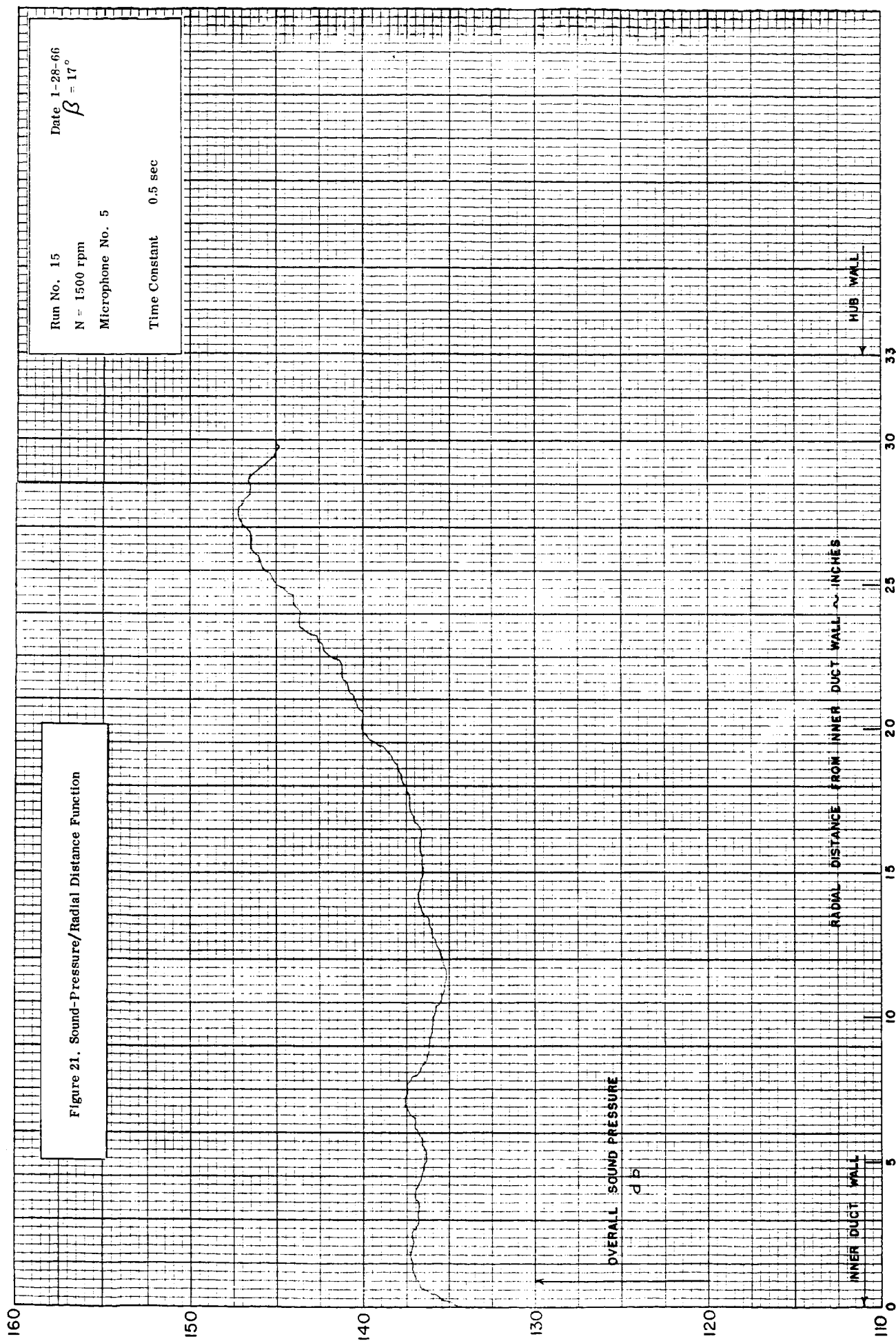
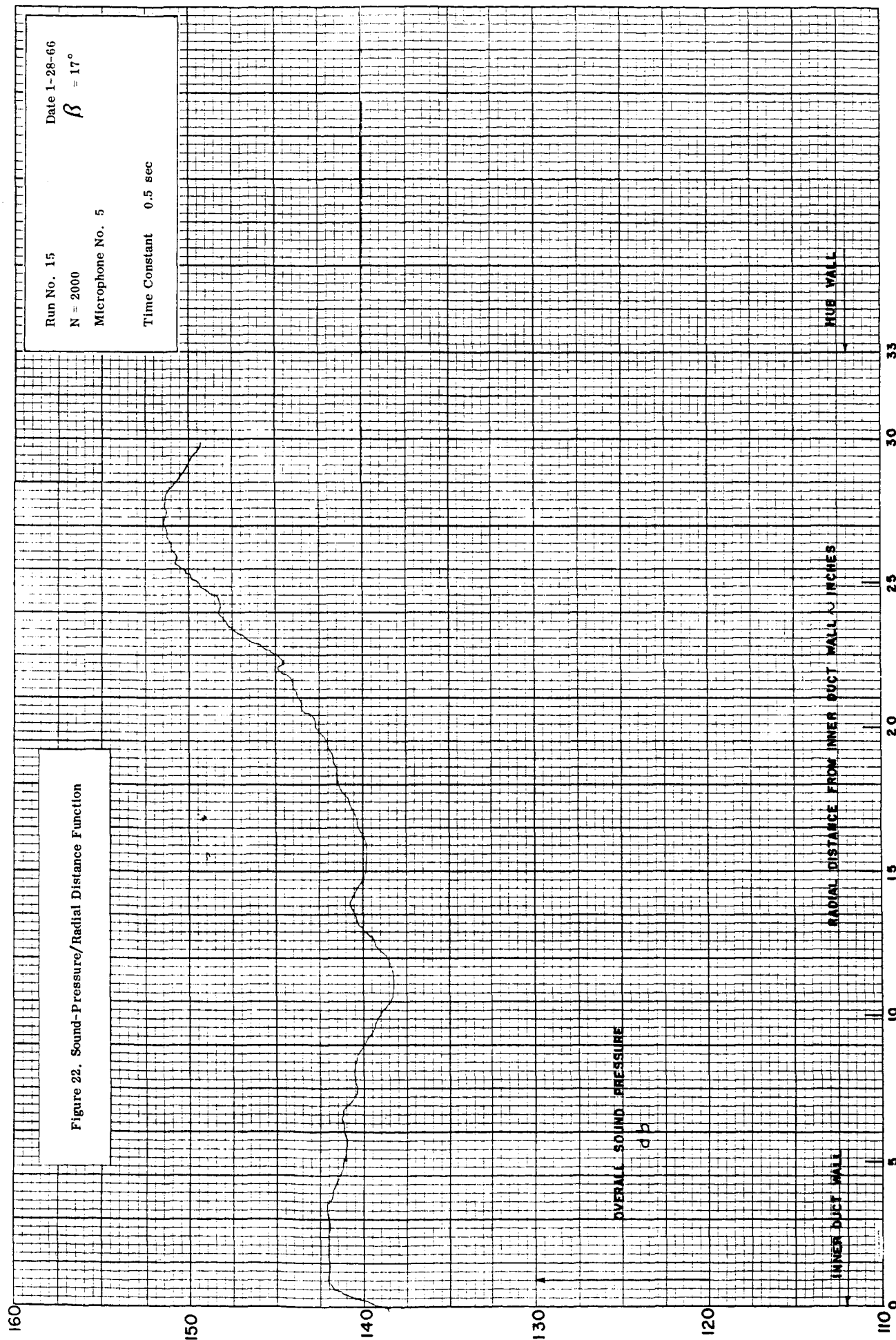
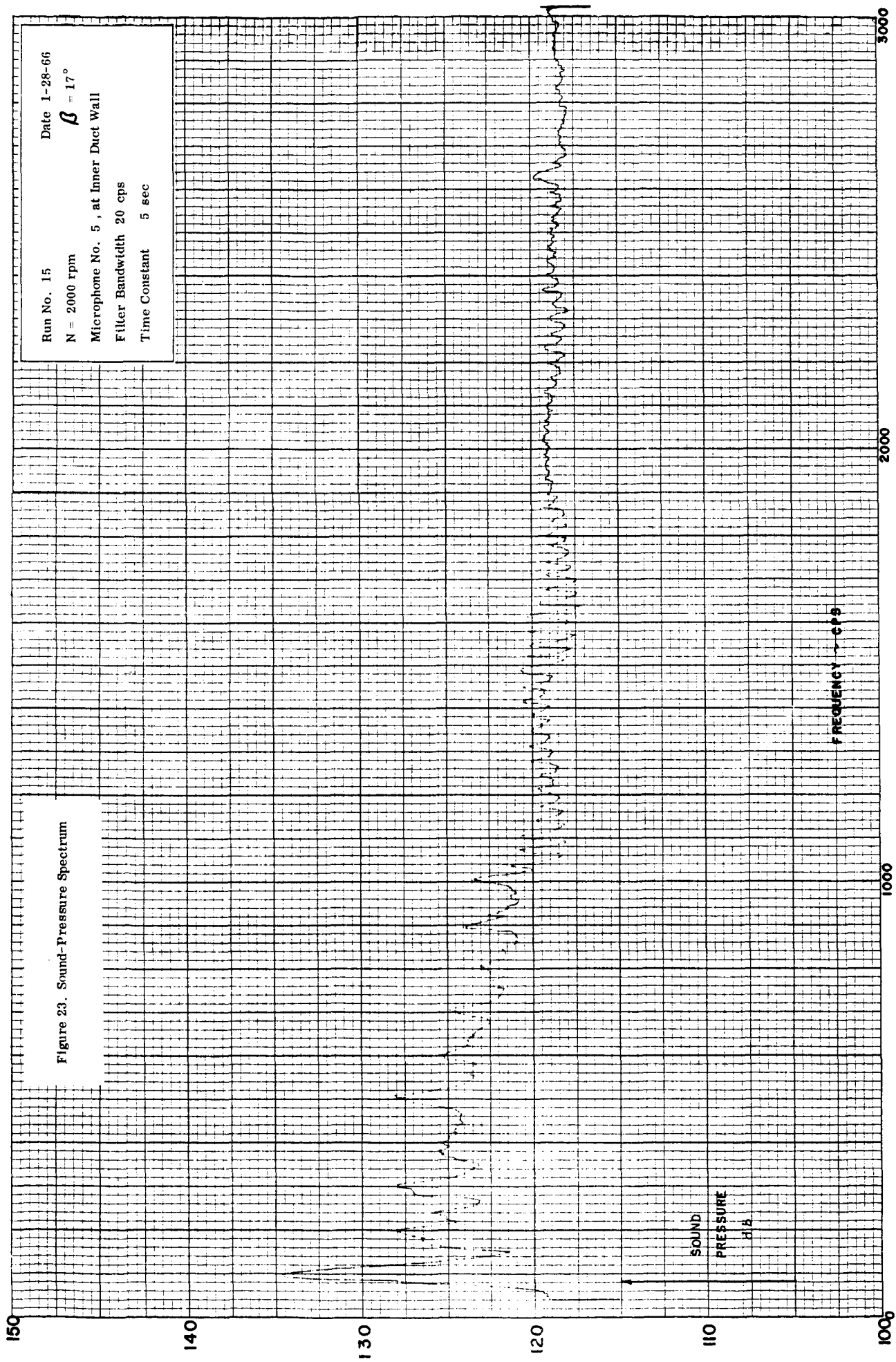
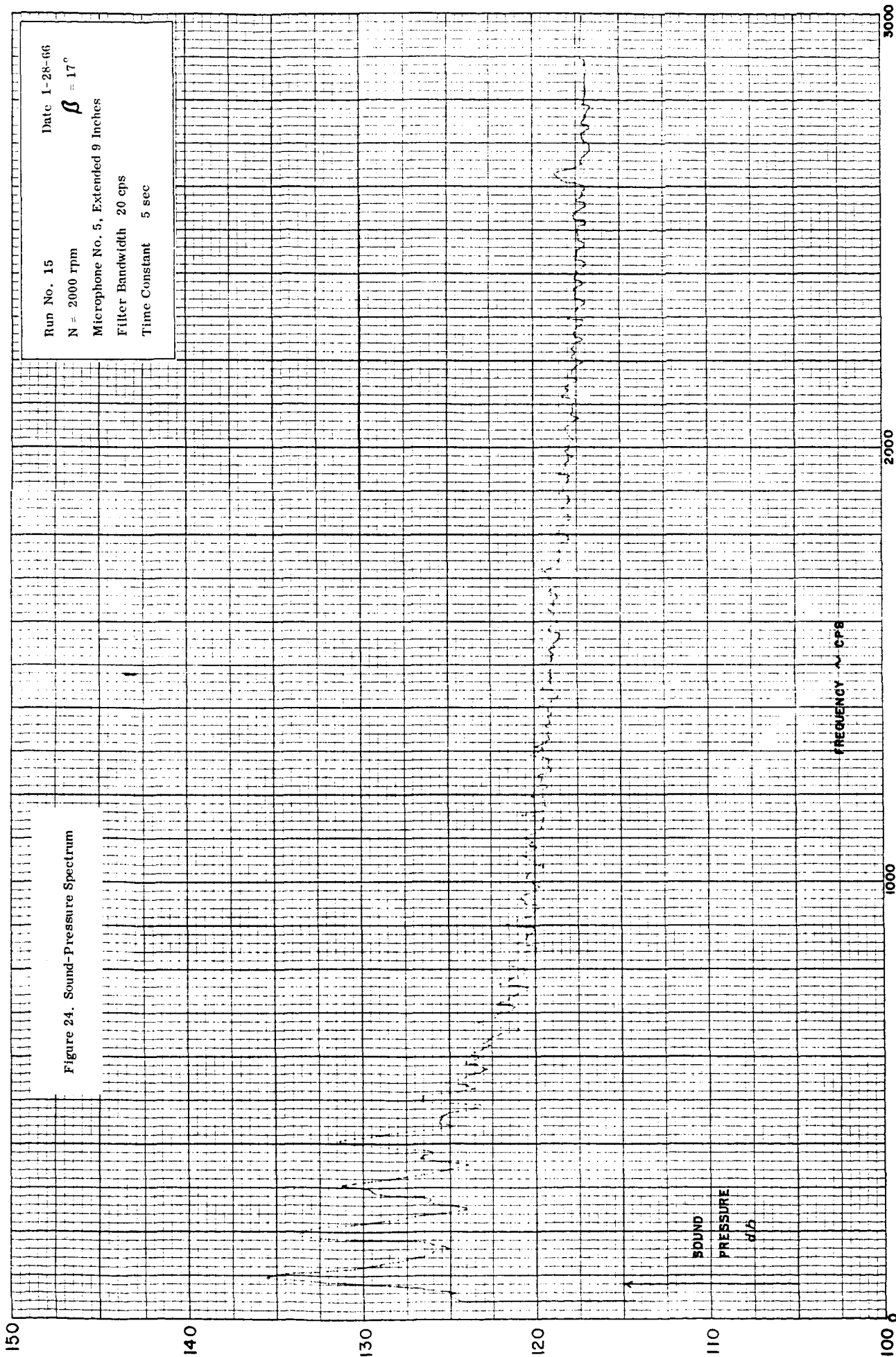


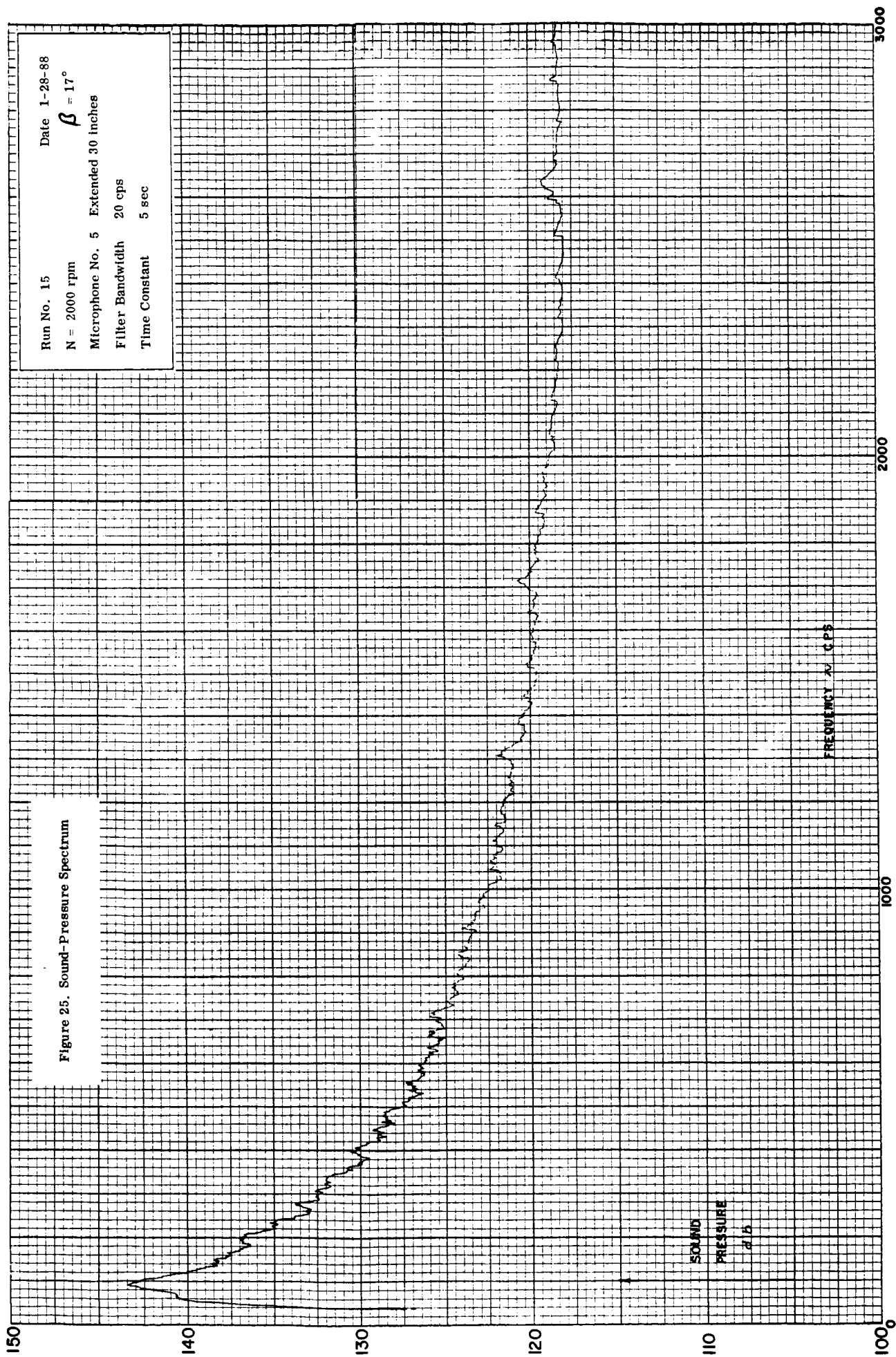
Figure 21. Sound-Pressure/Radial Distance Function

Run No. 15
 N = 1500 rpm
 Microphone No. 5
 Time Constant 0.5 sec
 Date 1-28-66
 $\beta = 17^\circ$









V. COMPARISON OF TEST RESULTS WITH THE CALCULATED VALUES

The overall sound pressure levels for test No. 6, 8, and 10 have been calculated, using as input the dimensions of the propeller and the values of propeller thrust, propeller power, and rotational speed obtained during the test phase. The dimensions of the three-blade propeller are as follows:

Propeller Diameter	7 ft
Hub Diameter	1.5 ft

For calculating the rms value of the overall sound pressure, the rms values of the first 10 harmonics were taken into account.

It can be seen from Figures 26, 27, and 28 that the recorded and calculated values at $\frac{x}{R_S} = 0$ (propeller plane) are in good agreement. The largest deviations did not exceed 2 db with the measured values always higher. This difference may be due to the simplifying assumption of a rectangular pressure distribution, made in the analysis. The actual pressure distribution is non-uniform with a maximum at a radial station near the tip, resulting in an increased sound pressure at the duct wall.

Because the decay term is a function only of the duct geometry and forcing frequency, being independent of the propeller loading, the same good agreement between analytical and test values is expected for the sound pressure distribution along the duct wall. This prediction is confirmed quite reasonably as shown by the values recorded with microphone No. 1 and No. 2 in front of the propeller plane. Behind the propeller plane, at microphone station No. 4 and No. 5, the deviations are sometimes higher. In one case (run No. 10, $N = 1000$), the difference is 6 db. The values recorded by microphone No. 6 indicate an increase if compared with the experimental values of microphone No. 5. This effect may be attributed to the change from a periodic to a random pressure field, found by the harmonic analysis and attributed to turbulence as discussed in Section IV.C.

Symbol	Prop. rpm (N)	Prop. shp	Prop. Thrust(lb)
○	1000	62.6	293.6
△	1500	202.3	642.9
□	2000	501.0	1174.6
◇	2200	679.0	1423.0

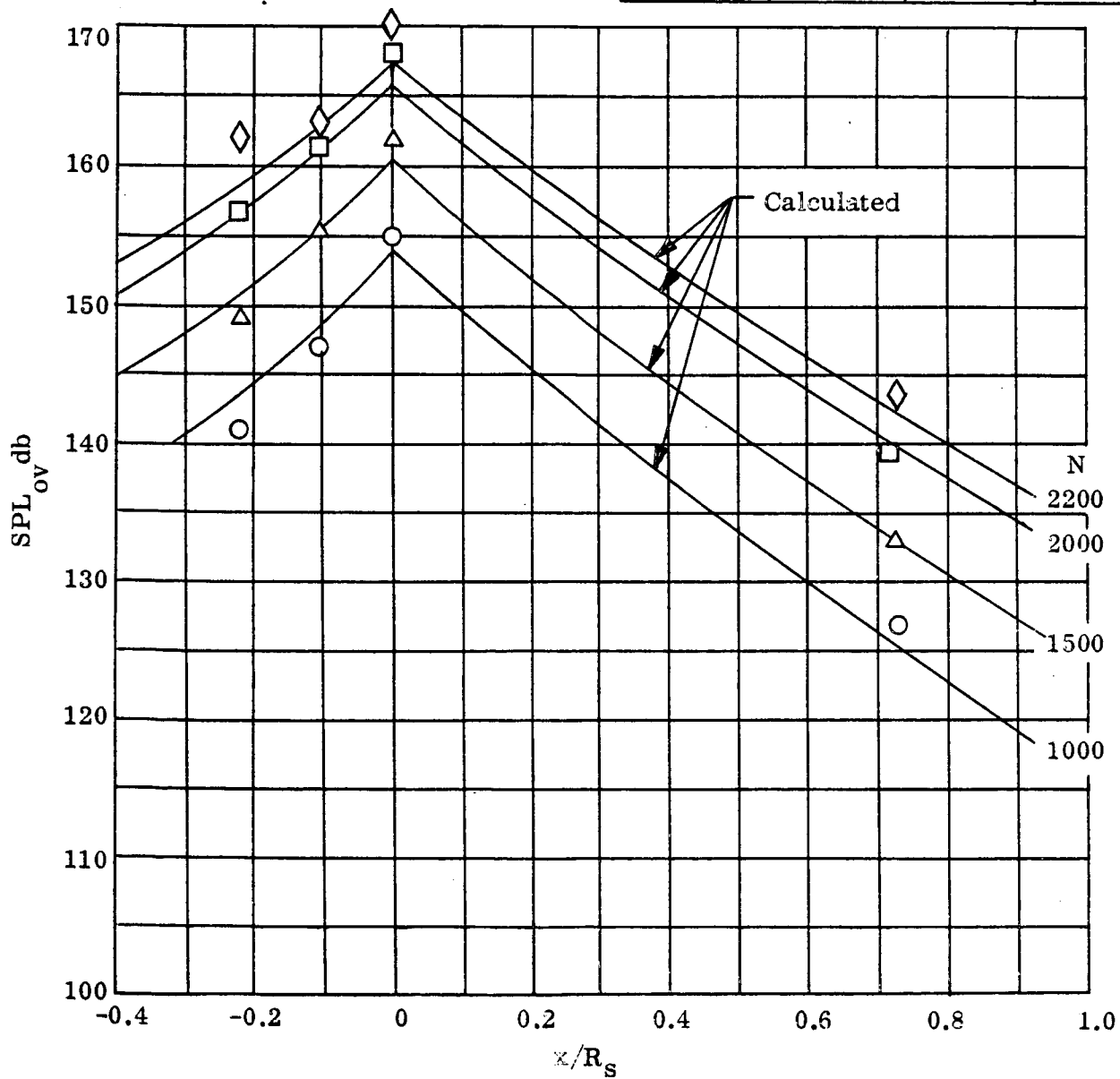


Figure 26. Sound Pressure Level Distribution along the Duct Inner Surface (Run No. 6, $\beta = 23^\circ$)

Symbol	Prop. rpm	Prop. shp	Prop. Thrust (lb)
⊙	1000	36.4	190.5
△	1500	119.3	419.7
□	2000	288.2	761.9
▽	2400	508.0	1111.0

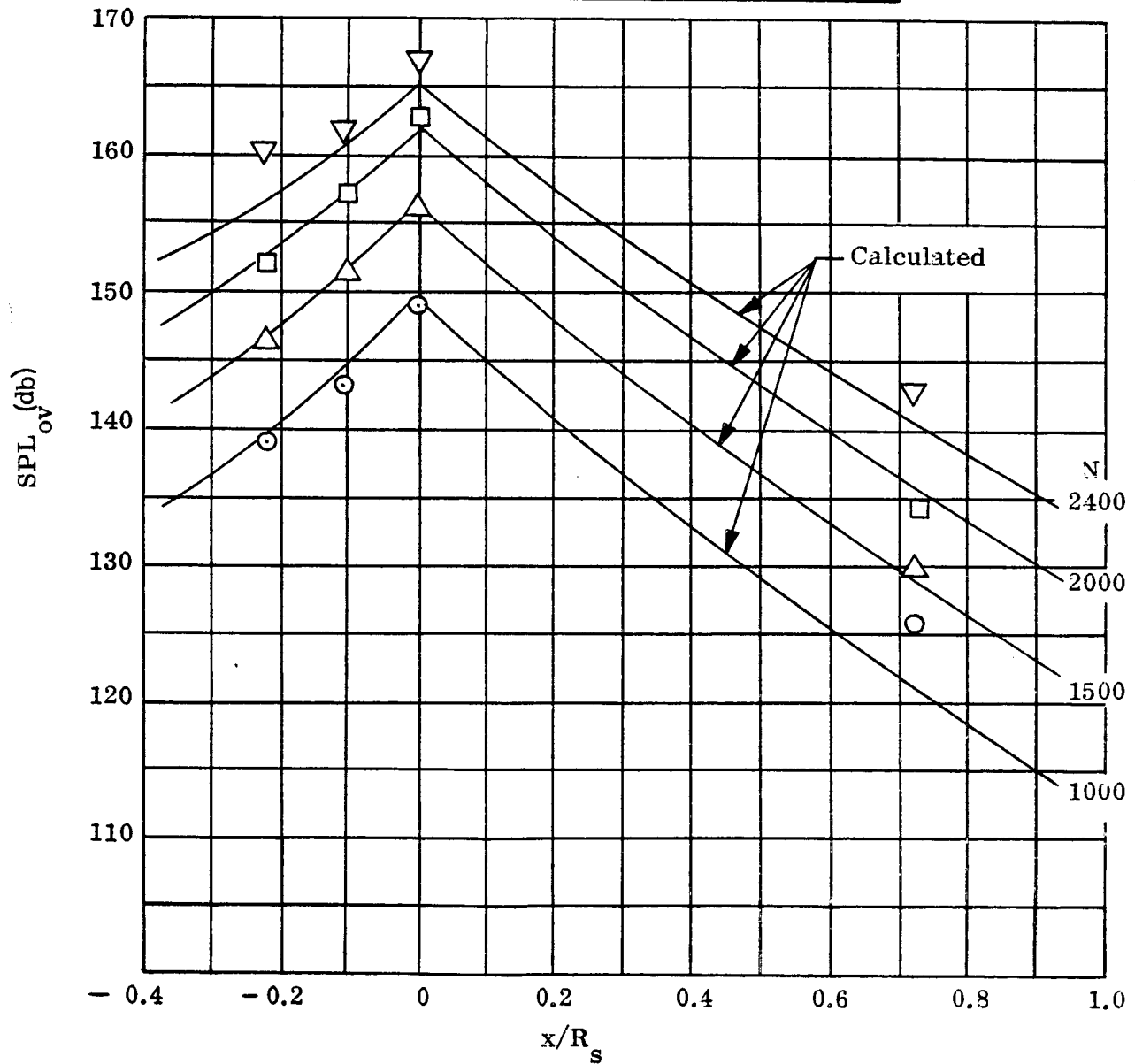


Figure 27. Sound Pressure Level Distribution along the Duct Inner Surface
(Run No. 8, $\beta = 17^\circ$)

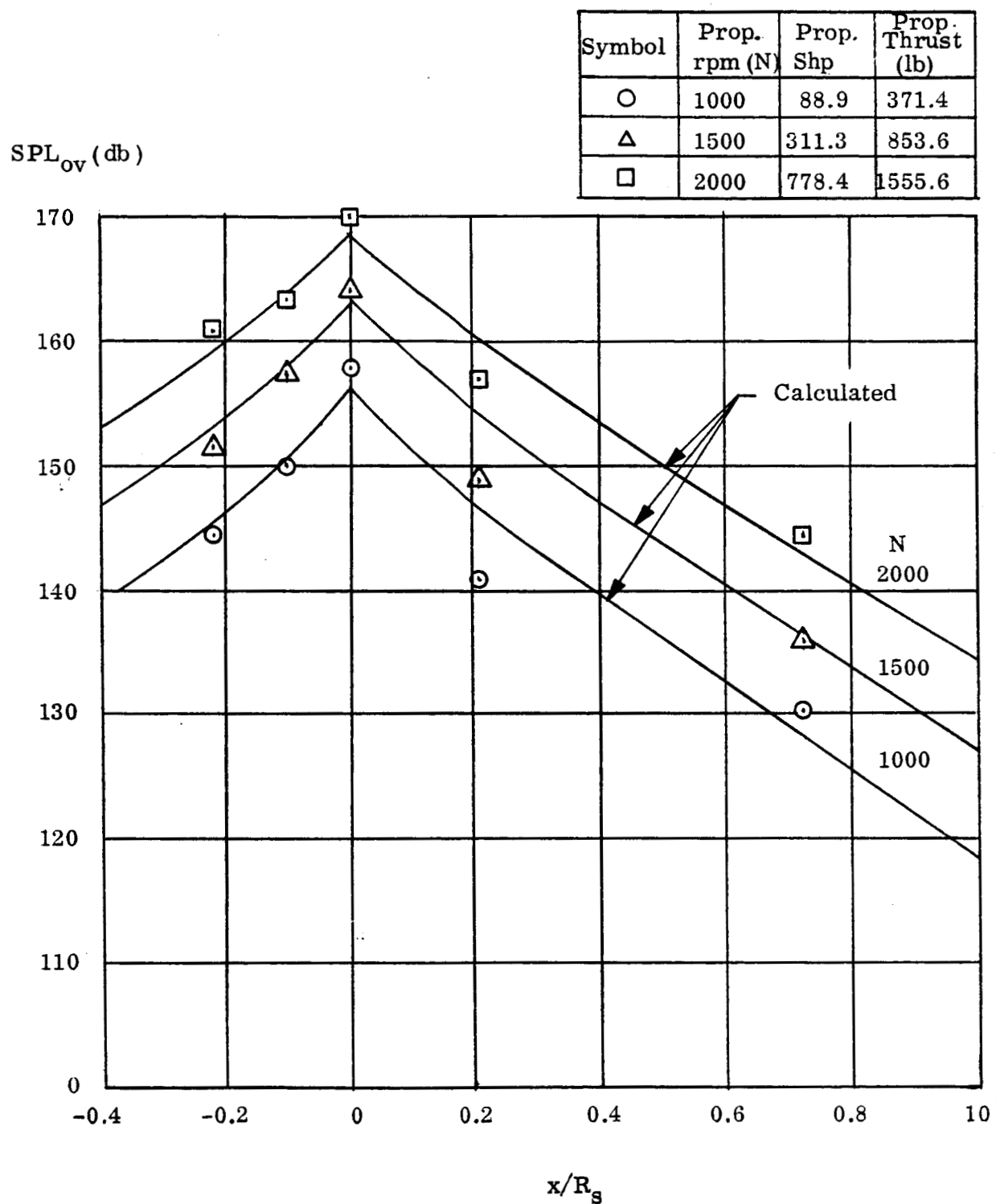


Figure 28. Sound Pressure Level Distribution Along the Duct Inner Surface (Run No. 10, $\beta = 29^\circ$)

As discussed in Section IV.E, a radial sound pressure distribution exploration was conducted during test No. 15. The calculated distribution, together with the recorded result, is plotted in Figure 29. Both curves have a similar form over the distance range from the wall surface to approximately $1/3$ of the propeller radius. The increase of the sound pressure during the last $2/3$ of the propeller radius might result from the considerable amount of turbulence found to exist in this region as discussed in Section IV.E.

For two runs (No. 8 and No. 10), the higher harmonics of the sound pressure were calculated and compared with the data of the harmonic analysis discussed in Section IV.C. The results are shown in Figures 30 and 31. The calculated values of the harmonics decay to a minimum amplitude at the eighth harmonic, followed by a rise that approaches the measured value at the tenth harmonic.

The differences between the calculated and measured sound pressure levels may be attributed to the assumed rectangular pressure distribution mentioned before.

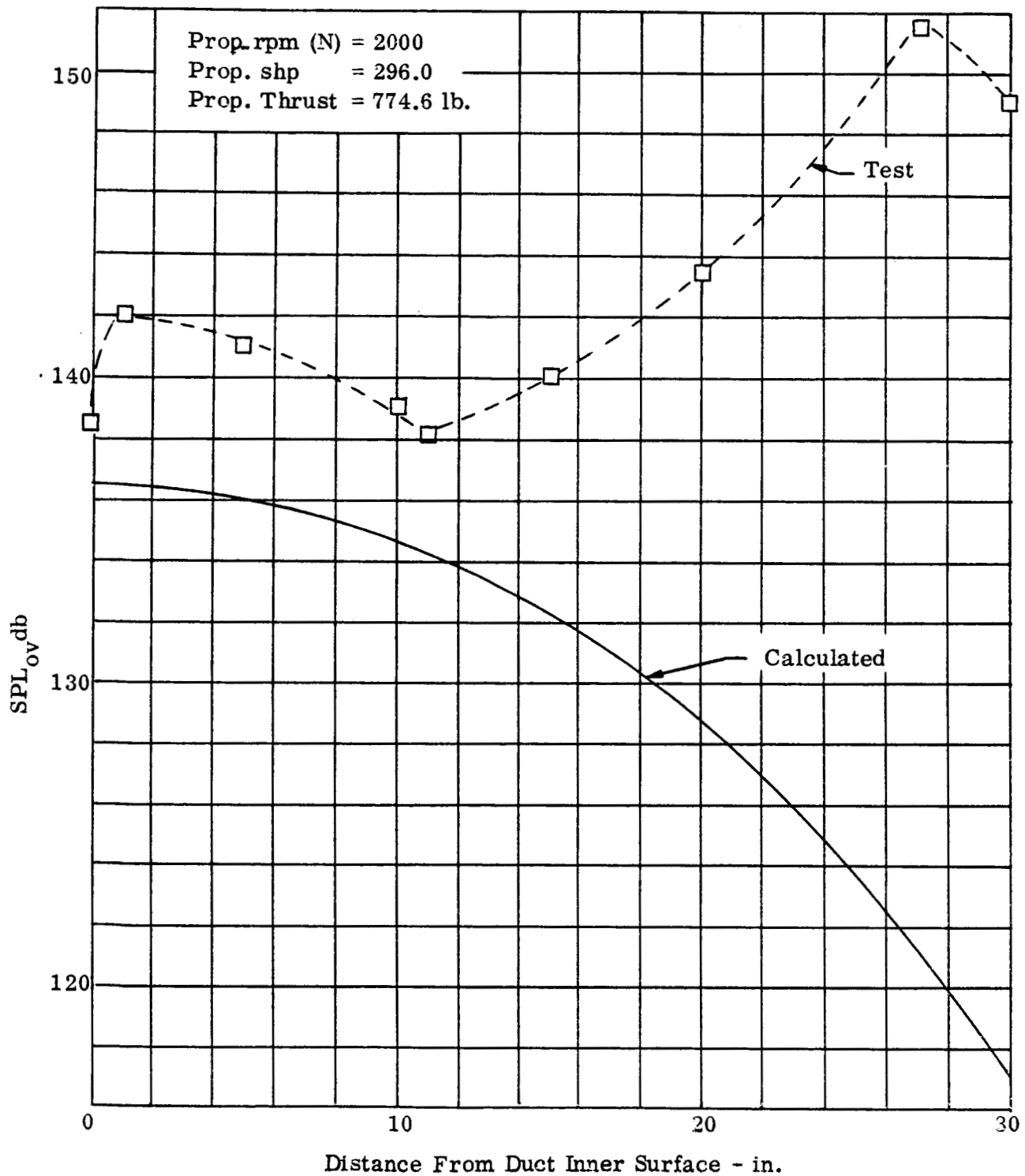


Figure 29. Radial Variation of Sound Pressure Level (Run No. 15, $\beta = 17^\circ$, Mic 5)

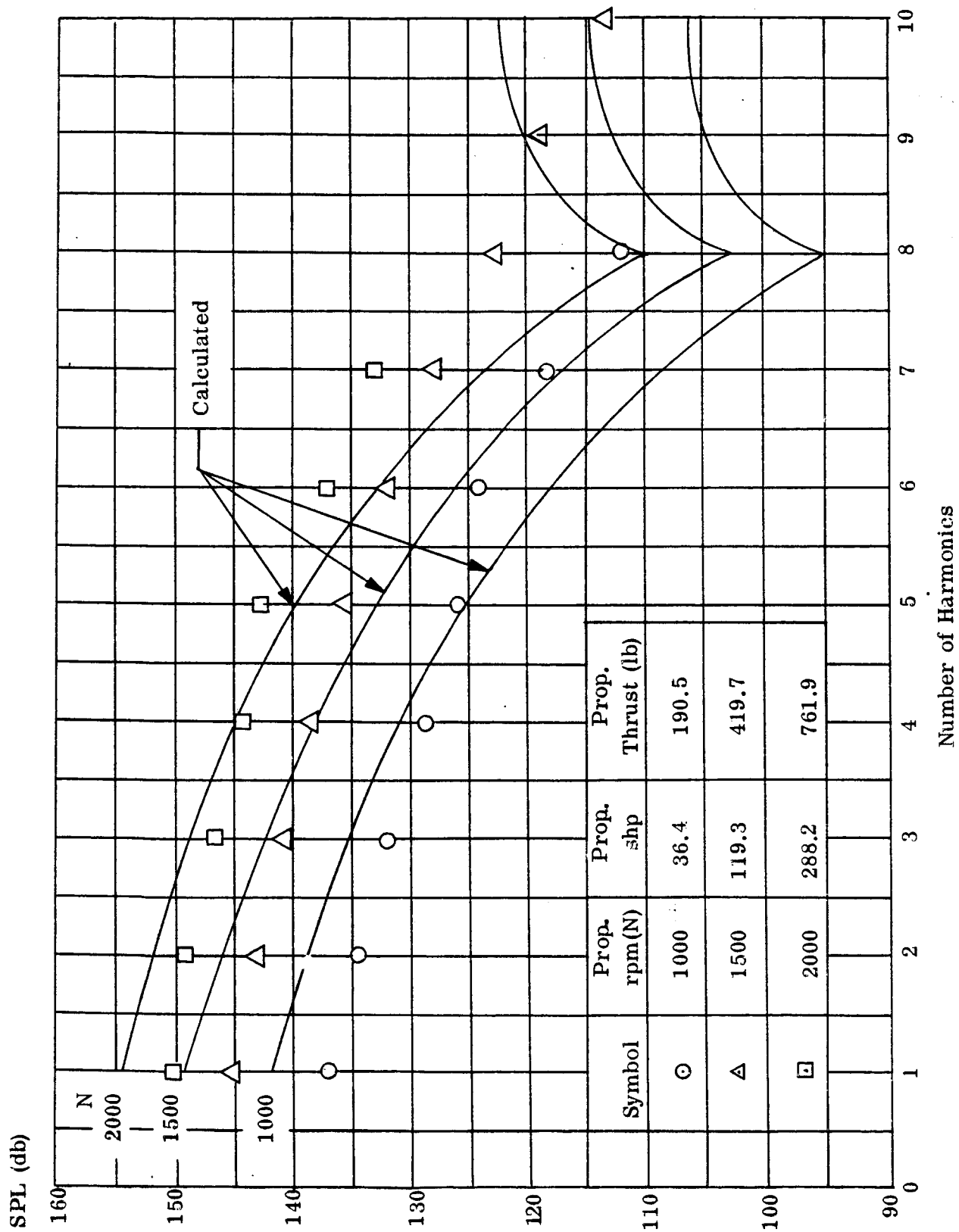


Figure 30. Harmonic Content (Run No. 8, $\beta = 17^\circ$, Mic No. 2)

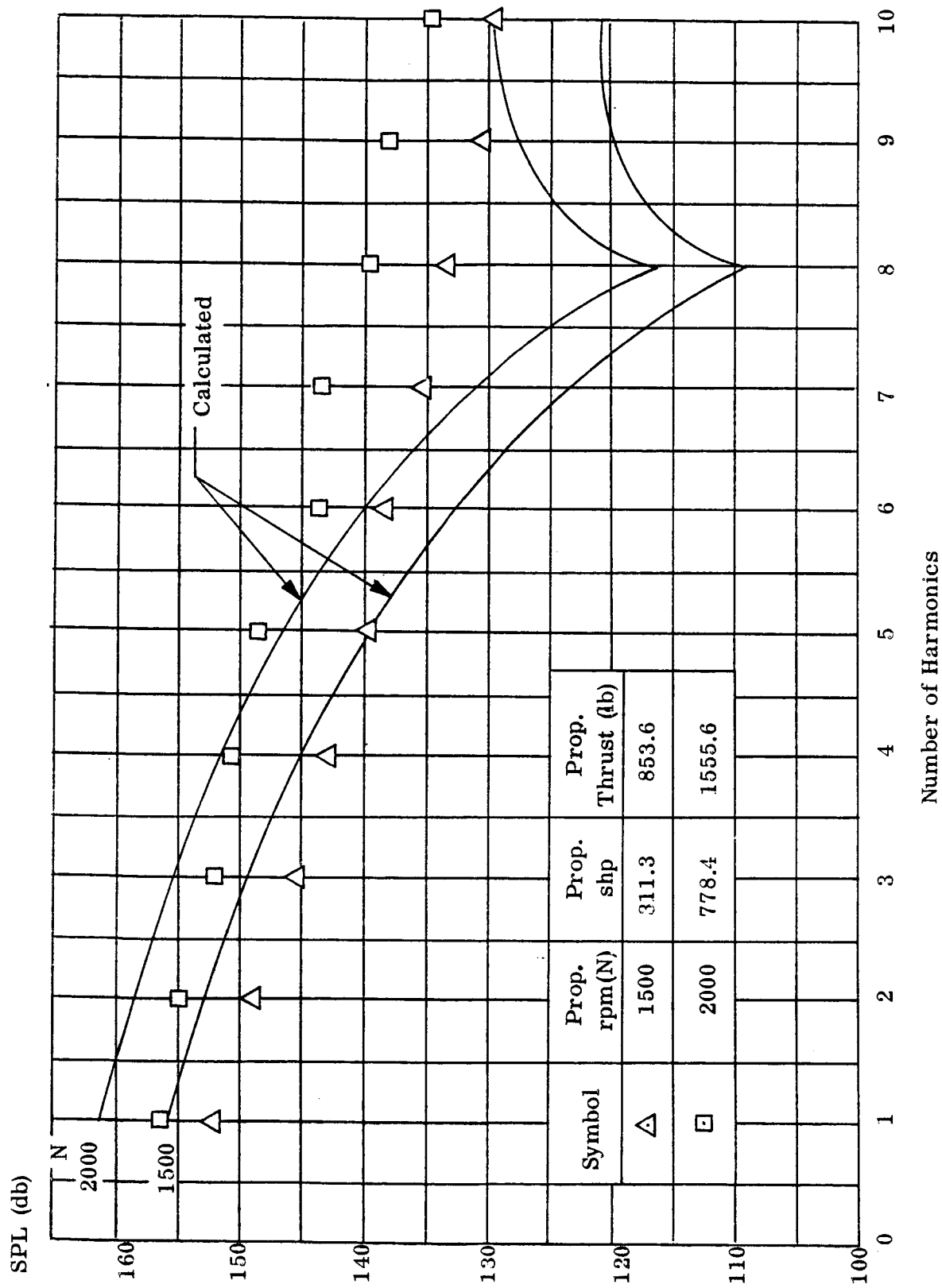


Figure 31. Harmonic Content (Run No. 10, $\beta = 29^\circ$, Mic. No. 2)

VI. CONCLUSIONS

1. The analytical method developed in this investigation permits the prediction of the overall rms-sound pressure distribution along the duct wall from measurable propulsion quantities. The demonstrated accuracy of the method is sufficient for design purposes. Since the method involves Bessel functions, the order of which is given by the product of the number of blades and the order of the harmonics, some difficulty in evaluation could arise with propellers having a larger number of blades (greater than four).
2. A harmonic analysis of the measured sound pressure fields in front and in the propeller plane yields line spectra consisting of harmonics of the blade passage frequency. A superposition of a random sound pressure field is evident aft of the propeller plane and may be attributed to turbulence from the propeller blades. This phenomenon requires further studies. The character of the different spectra may be important for predicting the excitation modes of the duct structure.
3. Variations of propeller tip clearance strongly affect the sound pressure field. Reducing the tip clearance results in a marked increase of the sound pressure particularly in the propeller plane. Further experimental work is required to obtain a relation between tip clearance and sound pressure field.
4. An exploration of the sound field in the radial direction aft of the propeller indicates an increase of the sound pressure with distance from the duct wall. This may be peculiar to the propeller operating condition, since the increased sound pressure would seem to be due to turbulence resulting from blade stall, a condition that would normally be avoided. However, this effect should not be neglected since it could influence the structural design of the hub.

VII. RECOMMENDATIONS

1. The expressions derived in the analytical approach are based on the assumption of a rectangular pressure distribution over the blades, and the differences between calculated and measured sound pressures are, for the most part, attributable to this simplified assumption. However, the actual pressure distribution differs from the rectangular distribution. This difference, in particular, influences the sound pressure field around the propeller tip. It is recommended that the present analysis be extended by taking into account more realistic pressure distribution to obtain a better agreement with the measured contribution of the higher harmonics.
2. As demonstrated, the experimental values do not allow the real distribution of the sound pressure at points close to the propeller plane to be determined. This area, however, is of particular interest to the design of acoustic fatigue resistant structures. Experience gained during propulsion tests of ducted propellers indicated that this area requires special attention. It is recommended, therefore, to explore the sound field in the region near the propeller plane, using a row of closely spaced microphones.
3. The propulsion quantity, propeller thrust, was calculated from the measured total thrust and, consequently, is subject to the inaccuracies of simple momentum theory. It is recommended, therefore, to improve the propulsion instrumentation required by providing redesigned load cells being developed by NASA-Ames, to be attached to the two ends of the main beam supporting the duct.
4. The tip clearance seems to have a strong influence on the sound pressure field, in particular in the propeller plane region. The data obtained from only one test cannot be considered as conclusive. A continuation of this test phase is recommended to be performed at several tip clearances and operational conditions, using the instrumentation outlined under point 3.

VIII. REFERENCES

1. A Theoretical Study of the Effect of Forward Speed on the Free-Space Sound Pressure Field Around Propellers, by J.E. Garrick and Charles E. Watkins, NACA Report 1198, 1954.
2. Oscillating Pressures Near a Static Pusher Propeller at Tip Mach Numbers up to 1.20 with Special Reference to the Effects of the Presence of the Wing, by Harvey H. Hubbard and Leslie W. Lassiter, NACA TN 3202, 1954.
3. Free-Space Oscillating Pressure Near the Tips of Rotating Propellers, by Harvey H. Hubbard and Arthur Regier, NACA TN 1970, 1949.
4. Axial Flow Compressor Noise Studies, by J.M. Tyler and T.G. Sofrin, S.A.E. 1961 Meeting, preprint 345D.
5. Compressor Noise Research, by David A. Bateman, Stephan C. Change, Bruce T. Hulse, and John B. Large; FAA-ADS-31, January, 1965.
6. Acoustical Fatigue Problems Associated with the Design of a Propeller Duct, by W. Fricke, J.R. Bissell, B.B. D'Ewart, Acoustic Fatigue in Aerospace Structures, 1965, Syracuse University Press. p. 685.

IX. APPENDIX.

A. INTRODUCTION

This section describes the analytical approach developed to obtain the calculated sound pressures presented in the main body of this report. The analytical development proceeds on the premise that the sound pressure field in the plane of the propeller may be adequately represented by expansion of the rotating net propeller blade pressure distribution in a suitable series. This series is a solution of the wave equation and satisfies the boundary conditions associated with the duct and hub.

A stationary type solution of the wave equation is obtained to both define the required series for the propeller plane pressures and the manner in which this field varies axially in the duct.

B. MODEL

Initially, the real propeller is replaced by an infinitely thin flat plate at an equivalent pitch angle (β_e) and zero tip clearance. This equivalent angle is obtained from the propeller thrust (T_p) and torque (Q):

$$\beta_e = \tan^{-1} \frac{Q}{\bar{r} T_p} \quad (1)$$

where \bar{r} is radial ordinate of the center of pressure.

The distribution of pressure over the blade is assumed to be constant and given by:

$$P_o = \frac{T_p}{B A_B \cos \beta_e} \quad (2)$$

where: B is the number of propeller blades

A_B is the propeller blade planform area

With the pressure P_0 determined from equations (1) and (2), the blade is now rotated to zero pitch, i.e., P_0 is everywhere normal to the propeller plane.

The blade planform selected for this study is a sector of a circle that is related to the real blade in that they both have the same geometric mean chord.

Finally, the above propeller is assumed to operate between two infinite concentric cylinders that represent the duct and hub.

The model described here was used to obtain the calculated sound pressures presented in the main body of this report. It is the least sophisticated model from which, it is believed, calculated pressures could be expected to be in good agreement with actual pressures. Other propeller blade pressure distributions and planforms may be assumed if a better compatibility between physical and mathematical models is desired.

C. SOLUTION

The wave equation in cylindrical coordinates is:

$$\frac{\partial^2 P}{\partial r^2} + \frac{1}{r} \frac{\partial P}{\partial r} + \frac{1}{r^2} \frac{\partial^2 P}{\partial \theta^2} + \frac{\partial^2 P}{\partial x^2} = \frac{1}{c^2} \frac{\partial^2 P}{\partial t^2} \quad (3)$$

The origin of the coordinate system is taken to be in the propeller plane. (See Figure 32.)

Since the pressure is associated with the rotating propeller blade pressure distribution, it must depend on a specific combination of the angular position (θ) and time ordinates, namely ($\theta - \omega t$), where ω is the angular velocity of the propeller. Therefore, a solution of the form

$$P_m = R_m(r) X_m(x) \cos [m(\theta - \omega t) + \phi_m] \quad (4)$$

is assumed.

Substituting from equation (4) in equation (3) gives:

$$\frac{1}{R_m} \left[\frac{d^2 R_m}{dr^2} + \frac{1}{r} \frac{d R_m}{dr} \right] - \frac{m^2}{r^2} + \frac{1}{X_m} \frac{d^2 X}{dx^2} = - \frac{m^2 \omega^2}{c^2} \quad (5)$$

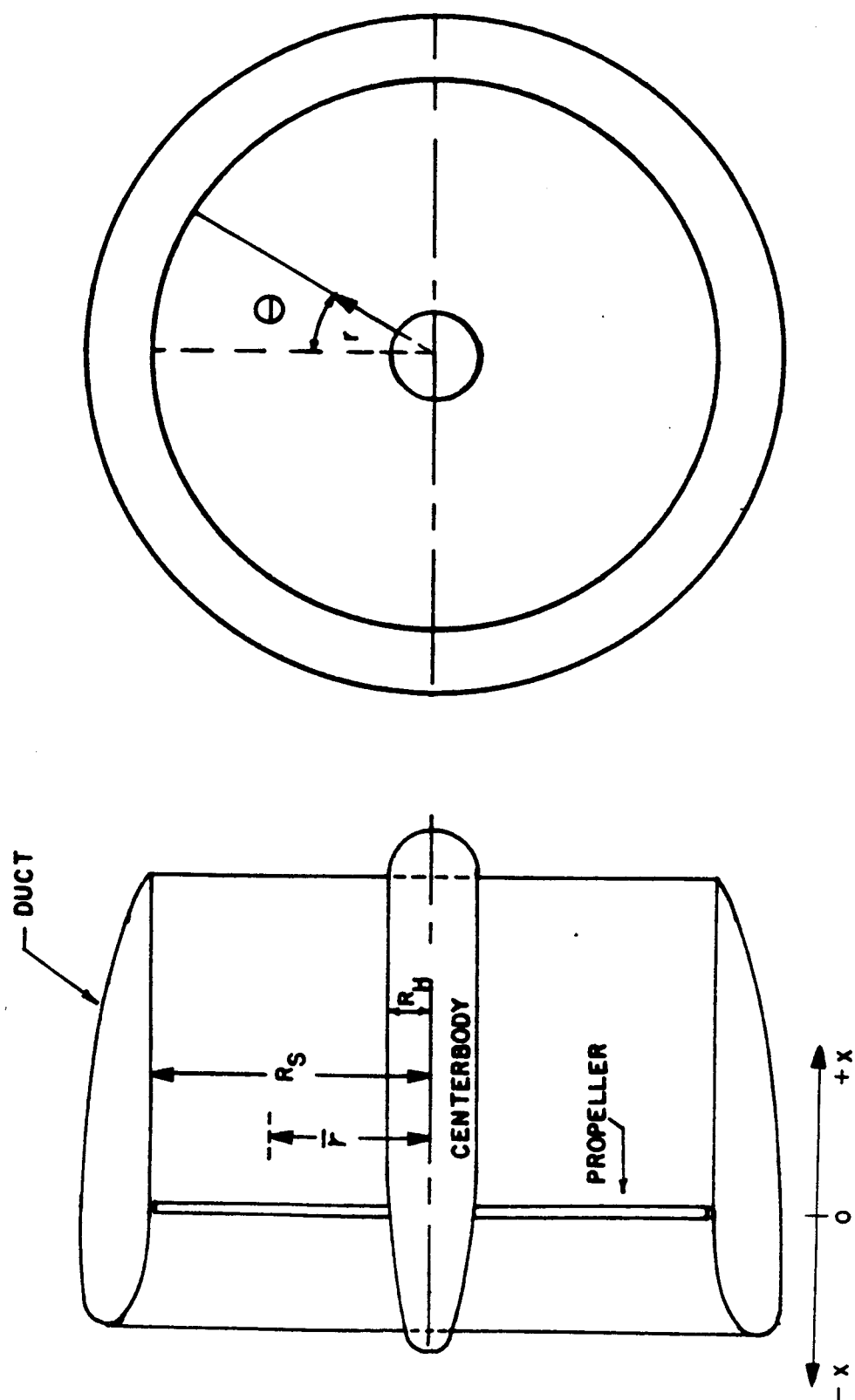


Figure 32. Propeller Disk and Coordinate System

and by the method of separation of variables we have:

$$\left. \begin{aligned} \frac{1}{R_m} \left[\frac{d^2 R_m}{dr^2} + \frac{1}{r} \frac{d R_m}{dr} \right] - \frac{m^2}{r^2} &= -k^2 \\ \frac{1}{X_m} \frac{d^2 X_m}{dx^2} &= -q^2, \quad k^2 + q^2 = \frac{m^2 \omega^2}{c^2} \end{aligned} \right\} \quad (6)$$

where k and q are nondimensional constants. The constants are referred to as separation constants and are here taken to be negative for convenience.

Solutions for equation (6) are:

$$\left. \begin{aligned} R_m &= A'_{mk} J_m(k_m r) + B'_{mk} Y_m(k_m r) = A_{mk} E_m(k_m r) \\ X_m &= ae^{ix\sqrt{\left(\frac{m\omega}{c}\right)^2 - k_m^2}} + be^{-ix\sqrt{\left(\frac{m\omega}{c}\right)^2 - k_m^2}} \end{aligned} \right\} \quad (7)$$

where

$$E_m = J_m + \frac{B'_{mk}}{A'_{mk}} Y_m$$

J_m = Bessel function of the first kind and order m .

Y_m = Bessel function of the second kind and order m .

If it is assumed that $X(x)$ is symmetrical with respect to the origin, then $a = b$ and the absolute value for x may be written.

Substituting from equation (7) in equation (2) gives:

$$\begin{aligned} P_m &= a_{mk} E_m(k_m r) \cos \left[m(\theta - \omega t) + \phi_m \right] e^{-|x|\sqrt{k_m^2 - \left(\frac{m\omega}{c}\right)^2}} \\ &= \left[\bar{a}_{mk} \cos m(\theta - \omega t) - \bar{b}_{mk} \sin m(\theta - \omega t) \right] E_m(k_m r) e^{-|x|\sqrt{k_m^2 - \left(\frac{m\omega}{c}\right)^2}} \end{aligned} \quad (8)$$

where,

$$\bar{a}_{mk} = a_{mk} \cos \phi_m, \quad \bar{b}_{mk} = a_{mk} \sin \phi_m$$

and,

$$a_{mk} = 2 a A_{mk}$$

The boundary condition associated with the duct and hub surfaces is that the pressure gradient be zero with respect to the normal at these surfaces. The characteristic number k is determined through this condition. Differentiating equation (8) with respect to r (which is in the same direction as the normal) and substituting for $r = R_S$ and $r = R_H$, respectively gives:

$$\left. \begin{aligned} J'_m(k_m R_S) + Q_{mk} Y'_m(k_m R_S) &= 0 \\ J'_m(k_m R_H) + Q_{mk} Y'_m(k_m R_H) &= 0 \end{aligned} \right\} \quad (9)$$

where $Q_{mk} = \frac{B'_{mk}}{A'_{mk}}$. Eliminating Q_{mk} from equation (9) gives

$$J'_m(k_m R_S) Y'_m(k_m R_H) - Y'_m(k_m R_S) J'_m(k_m R_H) = 0 \quad (10)$$

For any assigned value of m there is an infinite number of real roots for equation (10), each one determining a corresponding value of k . If μ denotes the rank of the root, values of k satisfying equation (10) will be written as $k_{m,\mu}$.

The complete solution for the sound pressure field in the duct may be written:

$$P = \sum_m \sum_{\mu} \left[\bar{a}_{m\mu} \cos m(\theta - \omega t) - \bar{b}_{m\mu} \sin m(\theta - \omega t) \right] \cdot E_m(k_{m\mu} r) e^{-|x| \sqrt{k_{m\mu}^2 - \left(\frac{m\omega}{c}\right)^2}} \quad (11)$$

It now remains to determine the coefficient $\bar{a}_{m\mu}$ and $\bar{b}_{m\mu}$.

Setting $x = 0$ in equation (11), multiplying both sides by $r \cos m\theta E_m(k_{m\mu} r)$ and integrating over the propeller disk area gives for any particular values of m and μ :

$$\int_0^{2\pi} \int_{R_H}^{R_S} P r \cos m \theta E_m(k_{m\mu} r) dr d\theta \quad (12)$$

$$= \int_0^{2\pi} \int_{R_H}^{R_S} \left[\bar{a}_{m\mu} \cos m(\theta - \omega t) - \bar{b}_{m\mu} \sin m(\theta - \omega t) \right] \cdot$$

$$r \cos m \theta E_m^2(k_{m\mu} r) dr d\theta$$

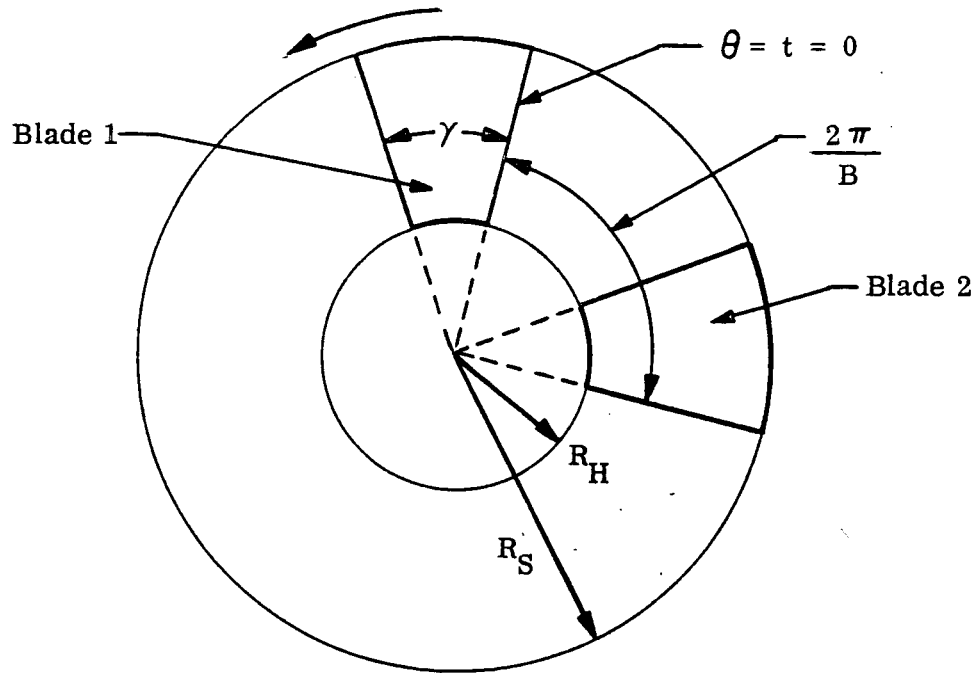
Looking first at the integrations with respect to θ , we find on the right-hand side

$$\begin{aligned} & \bar{a}_{m\mu} \int_0^{2\pi} \cos m(\theta - \omega t) \cos m \theta d\theta \\ &= \bar{a}_{m\mu} \int_0^{2\pi} \left[\cos^2 m \theta \cos m \omega t + \sin m \theta \cos m \theta \sin m \omega t \right] d\theta \\ &= \pi \bar{a}_{m\mu} \cos m \omega t \end{aligned} \quad (13)$$

and,

$$\begin{aligned} & -\bar{b}_{m\mu} \int_0^{2\pi} \sin m(\theta - \omega t) \cos m \theta d\theta \\ &= -\bar{b}_{m\mu} \int_0^{2\pi} \left[\cos m \theta \sin m \theta \cos m \omega t - \cos^2 m \theta \sin m \theta \sin m \omega t \right] d\theta \\ &= \pi \bar{b}_{m\mu} \sin m \omega t \end{aligned} \quad (14)$$

On the left-hand side of equation (12), the quantity P is zero except in the regions occupied by the propeller blades. In these regions, P is considered to have a constant value P_0 . Thus, to fix the limits of the θ -integration in a compatible manner, assume that θ and the time origins are coincident; i.e., initially $\theta = 0$ when $t = 0$ and that the angle θ is measured from the trailing edge of the sector representing, say blade 1, as indicated in the sketch below.



From the beginning of time, the blades turn at a constant angular velocity ω so that at any time t after the start of time, the trailing edge of blade 1 is at the angular position ωt , that of blade 2 is at $(\omega t - \frac{2\pi}{B})$, blade 3 is at $(\omega t - \frac{4\pi}{B})$ etc.

Hence, the θ -integration on the left of equation (12) can be written as the following summation:

$$\int_0^{2\pi} P \cos m\theta \, d\theta = \sum_{p=1}^B P_0 \int_{\omega t - (p-1)\frac{2\pi}{B}}^{\omega t - (p-1)\frac{2\pi}{B} + \gamma} \cos m\theta \, d\theta \quad (15)$$

and evaluated to give

$$\int_0^{2\pi} P \cos m\theta \, d\theta = \frac{2 BP_0}{m} \left[\cos m\omega t \cos \frac{m\gamma}{2} - \sin \omega t \sin \frac{m\gamma}{2} \right] \sin \frac{m\gamma}{2} \quad (16)$$

Substituting the results given in equations (13), (14), and (16) into equation (12) gives

$$\begin{aligned} & \frac{2 BP_0}{m} \left[\cos m\omega t \cos \frac{m\gamma}{2} - \sin \omega t \sin \frac{m\gamma}{2} \right] \sin \frac{m\gamma}{2} \int_{R_H}^{R_S} E_m(k_{m\mu} r) \, r dr \\ &= \pi \left[\bar{a}_{m\mu} \cos m\omega t + \bar{b}_{m\mu} \sin m\omega t \right] \int_{R_H}^{R_S} \left[E_m(k_{m\mu} r) \right]^2 r dr \quad (17) \end{aligned}$$

By equating coefficients of $\cos m\omega t$ and of $\sin m\omega t$, we obtain appropriate expressions for $\bar{a}_{m\mu}$ and $\bar{b}_{m\mu}$, namely

$$\bar{a}_{m\mu} = \frac{BP_0}{m\pi} \sin m\gamma \frac{\int_{R_H}^{R_S} E_m(k_{m\mu} r) \, r dr}{\int_{R_H}^{R_S} \left[E_m(k_{m\mu} r) \right]^2 r dr} \quad (18)$$

and

$$\bar{b}_{m\mu} = -\frac{BP_o}{m\pi} (1 - \cos m\gamma) \frac{\int_{R_H}^{R_S} E_m(k_{m\mu} r) r dr}{\int_{R_H}^{R_S} [E_m(k_{m\mu} r)]^2 r dr} \quad (19)$$

The integrals in the denominator may be evaluated and the final expressions are:

$$\begin{aligned} \bar{a}_{m\mu} &= \frac{2 BP_o \sin \gamma m}{m\pi \left[R_S^2 \left(1 - \frac{m^2}{k_{m\mu}^2 R_S^2}\right) E_m^2(k_{m\mu} R_S) - R_H^2 \left(1 - \frac{m^2}{k_{m\mu}^2 R_H^2}\right) E_m^2(k_{m\mu} R_H) \right]} \cdot \\ &\quad \int_{R_H}^{R_S} r E_m(k_{m\mu} r) dr \quad (20) \\ \bar{b}_{m\mu} &= \frac{2 BP_o [\cos \gamma m - 1]}{m\pi \left[R_S^2 \left(1 - \frac{m^2}{k_{m\mu}^2 R_S^2}\right) E_m^2(k_{m\mu} R_S) - R_H^2 \left(1 - \frac{m^2}{k_{m\mu}^2 R_H^2}\right) E_m^2(k_{m\mu} R_H) \right]} \cdot \\ &\quad \int_{R_H}^{R_S} r E_m(k_{m\mu} r) dr \end{aligned}$$

The remaining integral is best evaluated by some numerical technique.

With $\bar{a}_{m\mu}$ and $\bar{b}_{m\mu}$ determined by equation (20), substitution in equation (11) gives the required sound pressure. The sound pressure level (SPL) is given by:

$$\text{SPL (db)} = 74 + 20 \log_{10} P \quad (21)$$

Of particular interest when comparing calculated and measured results is the Root-Mean-Square (rms) values of the pressures. The rms value of the n^{th} harmonic is from equation (11):

$$(P_m)_{\text{rms}} = \left\{ \sum_{\mu=0}^{\infty} \frac{1}{2} (\bar{a}_{m\mu}^2 + \bar{b}_{m\mu}^2) E_m^2 (k_{m\mu} r) e^{-2|x| \sqrt{k_{m\mu}^2 - \left(\frac{m\omega}{c}\right)^2}} \right\}^{1/2} \quad (22)$$

since $m = nB$. The rms value of the total sound pressure is given by:

$$P_{\text{rms}} = \left[\sum_m (P_m)_{\text{rms}}^2 \right]^{1/2} \quad (23)$$

Substituting $(P_m)_{\text{rms}}$ or P_{rms} for P in equation (21) gives the corresponding sound pressure levels (SPL).

D. SOME AIDS TO EVALUATION

The calculated sound pressures of this report were obtained by summarizing the series over 10 values of n ($n = 1$ to 10) and four values of μ ($\mu = 0$ to 3). For this range of m and μ , Table I gives values of $k_{m\mu}$ and $Q_{m\mu}$. Since $k_{m\mu}$ and $Q_{m\mu}$ are functions only of the duct and hub geometrics, Table I may be used to calculate any or all of the theoretical pressures of this report.

TABLE I
CHARACTERISTIC NUMBERS AND COEFFICIENTS FOR
BESSEL FUNCTIONS

m	μ	$k_{m\mu}$	$Q_{m\mu}$
3	0	1.19955	-0.00169
	1	2.27151	-0.05965
	2	3.16154	-0.27592
	3	4.03937	-0.46739
6	0	2.14322	-0.00000
	1	3.35275	-0.00028
	2	4.36097	-0.00438
	3	5.31551	-0.03135
9	0	3.06041	0
	1	4.36767	0
	2	5.42988	-0.00002
	3	6.42888	-0.00031
12	0	3.96538	0
	1	5.35546	0
	2	6.46551	0
	3	7.49887	0
15	0	4.86295	0
	1	6.32636	0
	2	7.47936	0
	3	8.54474	0

m	μ	$k_{m\mu}$	$Q_{m\mu}$
18	0	5.75559	0
	1	7.28445	0
	2	8.47718	0
	3	9.57255	0
21	0	6.64367	0
	1	8.23303	0
	2	9.46262	0
	3	10.58618	0
24	0	7.53295	0
	1	9.17409	0
	2	10.43812	0
	3	11.58833	0
27	0	8.40895	0
	1	10.10901	0
	2	11.40545	0
	3	12.58092	0
30	0	9.29032	0
	1	11.03892	0
	2	12.36591	0
	3	13.56543	0

To provide an intermediate check, the coefficients $\bar{a}_{m\mu}$ and $\bar{b}_{m\mu}$ for the first five harmonics and the conditions of test run number 10 are provided in Table II.

Test Run No. 10

Conditions:

$$T_p = 1556 \text{ lb}$$

$$\text{SHP} = 778.4$$

$$N = 2000 \text{ rpm}$$

$$\gamma = 0.27 \text{ radian}$$

$$R_S = 3.5 \text{ ft}$$

$$R_H = 0.733 \text{ ft}$$

$$B = 3$$

TABLE II
FOURIER - BESSEL COEFFICIENTS

m	μ	$\bar{a}_{m\mu}$	$\bar{b}_{m\mu}$
3	0	257.04	-110.19
	1	115.15	- 49.363
	2	63.518	- 27.230
	3	33.012	- 14.152
6	0	228.22	-239.74
	1	118.95	-124.95
	2	81.228	- 85.326
	3	66.168	- 69.506
9	0	115.25	-310.14
	1	63.445	-170.72
	2	44.351	-119.35
	3	36.838	- 99.131
12	0	- 14.423	-292.89
	1	- 8.1943	-166.40
	2	- 5.8174	-118.14
	3	- 4.8940	- 99.385
15	0	-100.289	-205.40
	1	- 58.112	-119.02
	2	- 41.739	- 85.487
	3	- 35.441	- 72.588